# Statistical Properties of Dayside Whistler-mode Waves at Low Latitudes Under Various Solar Wind Conditions

**Y. Peng[1], W. Li[1], Q. Ma[1,2] and X.-C. Shen[1]**

[1]Center for Space Physics, Boston University, Boston, MA, USA.

[2]Department of Atmospheric and Oceanic Sciences, University of California Los Angeles, CA, USA

Corresponding author: Wen Li (luckymoon761@gmail.com)

**Key Points:**

- We conduct an 8-year survey on the distributions of dayside whistler-mode waves and 1-20 keV electrons using THEMIS data.
- Whistler wave amplitude, electron anisotropy, and PSD increase with rising solar wind dynamic pressure and AE index from dawn to noon.
- Statistical results show that dayside waves are generated near the equator, with propagation needed to explain waves at higher latitudes.

## Abstract

While whistler-mode waves are generated by injected anisotropic electrons on the nightside, the observed day-night asymmetry of wave distributions raises an intriguing question about their generation on the dayside. In this study, we evaluate the distributions of whistler-mode wave amplitudes and electrons as a function of distance from the magnetopause on the dayside from 6 h to 18 h in magnetic local time (MLT) within ±18° of magnetic latitude using the Time History of Events and Macroscale Interaction During Substorms (THEMIS) measurements from June 2010 to August 2018. Specifically, under different levels of solar wind dynamic pressure and geomagnetic index, we conduct a statistical analysis to examine whistler-mode wave amplitude, as well as anisotropy and phase space density (PSD) of source electrons across 1–20 keV energies, which potentially provide a source of free energy for wave generation. In coordinates relative to the magnetopause, we find that lower-band (0.05–0.5 $f_{ce}$) waves occur much closer to the magnetopause than upper-band (0.5–0.8 $f_{ce}$) waves, where $f_{ce}$ is electron cyclotron frequency. Our statistical results reveal that strong waves are associated with high anisotropy and high PSD of source electrons near the equator, indicating a preferred region for local wave generation on the dayside. Over 10–14 h in MLT, as latitude increases, electron anisotropy decreases, while whistler-mode wave amplitudes increase, suggesting that wave propagation from the equator to higher latitudes, along with amplification along the propagation path, is necessary to explain the observed waves on the dayside.

## 1 Introduction

Whistler-mode waves, which are right-hand circularly polarized electromagnetic emissions, play a crucial role in energetic electron dynamics in the magnetosphere. These waves affect the dynamics of energetic electrons through resonant interactions, contributing to the acceleration of radiation belt electrons (Chen et al., 2007; Horne et al., 2005; Thorne et al., 2013) and producing diffuse and pulsating aurora (Nishimura et al., 2010; Thorne et al., 2010). Therefore, it is essential to understand the critical parameters responsible for the generation and propagation of whistler-mode waves.

Whistler-mode waves in the Earth's magnetosphere are categorized into several types, including, but not limited to, chorus waves, hiss waves and lightning-generated whistlers (LGWs). Hiss waves, which are present inside the plasmasphere or high-density plumes, are often incoherent and broadband emissions with a frequency range from ~100 Hz to ~2 kHz (Meredith et al., 2004; Thorne et al., 1973). In contrast to chorus waves (Li et al., 2010; Meredith et al., 2012), which are typically observed from the midnight to the afternoon sector, hiss waves preferentially occur on the dayside (Meredith et al., 2006). The generation of hiss remains an active area of research. The unstable electron distributions within the plasmasphere provide preferential amplification for hiss in the equatorial region (Church & Thorne, 1983; Solomon et al., 1988). Previous studies suggest that LGWs can evolve into hiss after several magnetospheric reflections (Draganov et al., 1992; Green et al., 2005). Moreover, whistler-mode chorus waves can propagate to higher latitudes, refract into the plasmasphere, and evolve into hiss (Bortnik et al., 2009, 2011; Chen et al., 2012a, 2012b).

Whistler-mode chorus waves typically consist of short coherent bursts with discrete elements of rising or falling tones (e.g., Zhang et al., 2020). They typically occur in two frequency bands: the lower band (0.05–0.5 $f_{ce}$) and the upper band (0.5–0.8 $f_{ce}$), where $f_{ce}$ is the equatorial electron cyclotron frequency (Burtis & Helliwell, 1969; Hayakawa et al., 1984; Koons

& Roeder, 1990; Tsurutani & Smith, 1977). Chorus emissions, especially on the nightside, are preferentially excited in low-density regions outside the plasmapause near the geomagnetic equator (Kennel & Petschek, 1966; Lauben et al., 2002; LeDocq et al., 1998; Omura et al., 2008; Santolík et al., 2003). Substorm injections provide favorable conditions by supplying anisotropic plasma sheet electrons, often referred to as source electrons, which are responsible for generating chorus waves and have energies from a few keV to tens of keV (Li et al., 2010). As these electrons drift eastward, the cyclotron instability continues to develop, leading to the extensive observation of chorus waves from the postmidnight sector through the dawn into the noon sector.

Previous studies have demonstrated a strong correlation between substorm injections and chorus waves from postmidnight to dawn (Abel et al., 2006; Li et al., 2008, 2010; Meredith et al., 2001, 2012; Smith et al., 1999; Thorne et al., 1977; Tsurutani & Smith, 1977). Nightside chorus waves are known to be confined to the equatorial plane within around 10° magnetic latitude, while dayside chorus waves can extend to much higher latitudes above 20° (Agapitov et al., 2018; Burton & Holzer, 1974; Li et al., 2009; Meredith et al., 2001, 2012). In the dayside outer magnetosphere near the magnetopause, the occurrence rate of chorus is even surprisingly higher than that in other regions and appears less dependent on substorm activity (Koons & Roeder, 1990; Li et al., 2009; Santolík et al., 2005). Tsurutani & Smith (1977) analyzed one-year data from the OGO-5 spacecraft in highly elliptical orbits and identified two favored regions for chorus: equatorial chorus at low L-shells on both the nightside and dayside, and dayside chorus at large L-shells and high magnetic latitudes, called "minimum B pockets."

Compared to the nightside chorus waves that are confined near the equator, dayside chorus waves tend to propagate to higher latitudes due to weaker Landau damping (e.g., Bortnik et al., 2006, 2007; Meredith et al., 2012). As a result, dayside chorus waves resonate with higher-energy electrons, leading to MeV microburst precipitation, which is critical for energetic electron losses in the magnetosphere (Horne et al., 2003; Li et al., 2007; Lorentzen et al., 2001; O'Brien et al., 2004). Previous studies suggest that chorus waves can be generated near the equator, propagate to high latitudes (Bortnik et al., 2007; Chen et al., 2013; Colpitts et al., 2020; Omura et al., 2008), and even reflect back to the equator under certain conditions (Agapitov et al., 2011; Breuillard et al., 2013; Chum & Santolík, 2015; Santolík et al., 2014). In addition, they can also be generated in minimum B pockets near the cusp (Pickett et al., 2001; Tsurutani & Smith, 1977; Vaivads et al., 2007).

Keika et al. (2012) observed a long-lasting chorus amplification event under near-zero dB/ds and quiet conditions in the dayside uniform zone, which is located between the near-Earth dipole zone and minimum B pockets. Using numerical experiments, Tao et al. (2014) demonstrated that the dayside uniform field configuration could significantly reduce the threshold for chorus generation, as the field configuration is essential for the effectiveness of nonlinear interactions between chorus waves and energetic electrons (Albert et al., 2000; Bortnik et al., 2008; Gan et al., 2020; Tao et al., 2014; Zhang et al., 2018). Consequently, it is believed that drift shell splitting and/or low magnetic field inhomogeneity play important roles in the extensive presence of dayside chorus (Agapitov et al., 2018; Li et al., 2010; Meredith et al., 2012; Spasojavic & Inan, 2010; Voshchepynets et al., 2024).

Our study focuses on a statistical survey of dayside whistler-mode wave distributions and their associated source electron distributions. To highlight the effect of magnetic field inhomogeneity, we use a new coordinate system based on the relative L-shell distance to the magnetopause location, instead of L-shell. In Section 2, we describe the wave and particle data from the Time History of Events and Macroscale Interaction during Substorms (THEMIS) spacecraft. The overall statistical surveys of chorus wave amplitude, electron phase space density, and electron anisotropy are presented in Section 3.1. Sections 3.2 and 3.3 analyze the response of these parameters to varying levels of solar wind dynamic pressure and geomagnetic activity. The key findings of our study are discussed and summarized in Sections 4 and 5.

## 2 THEMIS Data Analysis

The THEMIS satellites, launched in 2007, have been orbiting in the near-equatorial plane with an apogee above 10 $R_E$ and a perigee below 2 $R_E$ (Angelopoulos, 2008). These orbits make them ideally suited for studying whistler-mode wave emissions in Earth's dayside magnetosphere. Electron measurements are obtained from the Electrostatic Analyzer (ESA) over an energy range from a few eV to 30 keV (McFadden et al., 2008). The wave power spectra data collected during the fast survey (fff mode) provides measurements with a time resolution down to 1 s and includes 32 or 64 bands logarithmically spaced across a frequency range of 4-4,000 Hz (Cully et al., 2008). The Fluxgate Magnetometer (FGM) (Auster et al., 2008) measures the background magnetic fields and low-frequency fluctuations. The total magnetic field magnitude obtained from FGM measurements is utilized to calculate the local electron cyclotron frequency.

We obtained the magnetic wave amplitudes of upper-band (UB) waves by integrating the fff data of magnetic spectral density over 0.5–0.8 $f_{ce}$. For lower-band (LB) waves, the frequency range is chosen from the higher value between 30 Hz and $f_{ce}/43$ (to avoid low frequency noise) to 0.5 $f_{ce}$. The value of $f_{ce}/43$ approximately corresponds to the lower hybrid resonance frequency ($f_{LH} \approx \sqrt{f_{ce} f_{cp}} \approx f_{ce}/43$, where $f_{cp}$ is proton cyclotron frequency). It is noteworthy that although most of the waves are chorus waves, the dataset also includes whistler-mode waves observed in the plumes, as no specific density criteria were used to exclude them. The solar wind dynamic pressure (Dp) and the geomagnetic auroral electrojet index (AE) values were obtained from the OMNI database with a 1-min resolution. The wave power spectrogram in fff mode has a time resolution of either 8 s or 1s. For statistical purposes, the OMNI data were interpolated to match the cadence of the wave data.

Among the five THEMIS satellites, two of them (Probes B and C) transitioned to orbiting the Moon after 2010 (Angelopoulos, 2011). Therefore, we utilize THEMIS A, D and E from June 2010 to August 2018 to investigate the dayside whistler-mode wave distributions under various conditions relative to the magnetopause. To identify the location of magnetopause from the THEMIS observation, we first divide the event interval into a half-orbit during which the satellite traverses across the magnetopause between its perigee and apogee. If the spacecraft is located at L > 8, the measured electron temperature ($T_e$) is less than 300 eV and the total ion velocity with a 15-minute running average subtracted ($V_i$) exceeds 30 km/s (Haaland et al., 2019), the measurement closest to Earth during each half-orbit is identified as the magnetopause. Regions with L-shells larger than the identified magnetopause location are classified being outside the magnetopause (flag = 2); otherwise, they are considered to be inside the magnetopause (flag = 1). To avoid misidentification due to local short-term variations in the space environment, we require flag = 2 to persist for at least 3 minutes. Our study focuses on the whistler-mode waves inside magnetopause and excludes those in the magnetosheath.

The modeled magnetopause is based on the model by Shue et al. (1997). Since the magnetopause location predicted by the Shue et al. (1997) model may be different from actual observation, we scaled the modeled magnetopause along the THEMIS half-orbit using the observed magnetopause location and the shape of the Shue et al. (1997) model:

$$sL_{MP}(t) = mL_{MP}(t)\frac{L_{MP}(t=t_0)}{mL_{MP}(t=t_0)}, \tag{1}$$

where $sL_{MP}$ is the scaled modeled magnetopause, $mL_{MP}$ is the modeled magnetopause, $t$ is the time of observation, and $t_0$ is the time at the observed magnetopause flag on the same half-orbit. Since the THEMIS probes may not always observe the magnetopause crossing on the dawn or dusk side, we implement $sL_{MP}$ for events where the observed magnetopause crossings occur on the dayside (8–16 MLT), and $mL_{MP}$ for the events when the magnetopause crossing was not observed. For simplicity, we use $L_{MP}$-L throughout the rest of the paper. We also tested the magnetopause location using only the Shue et al. (1997) model and found that the statistical results (Figures 2–8) closely align with the present results.

Figure 1 shows an event observed by THEMIS D over 1000–1600 UT on 15 December 2012. During this event, THEMIS D moved from an L-shell of 3.7 to 10.6, crossing the magnetopause at ~12.7 MLT, as shown in Figure 1b. The interpolated values of Dp and AE are shown in Figure 1a. Figure 1c shows various L-shell parameters: the L-shell of the satellite is depicted by the red solid line, the distance from the satellite to the modeled magnetopause ($mL_{MP}$-L) by the orange solid line, and the distance to the scaled magnetopause ($sL_{MP}$-L) by the blue dashed line. The modeled magnetopause closely matches the observation, so $mL_{MP}$ is nearly identical to $sL_{MP}$ during this event. Figure 1d presents the total electron density inferred from the spacecraft potential, confirming the identification of magnetopause location. Figure 1e shows the wave magnetic spectral density, with white lines representing electron cyclotron frequency ($f_{ce}$), half and 0.05 times of local $f_{ce}$. Figure 1f shows the spin-averaged magnetic wave amplitudes integrated from the power spectral density. The strongest lower-band (LB) whistler-mode waves, shown by the black line, were observed closer to the magnetopause (MP), while upper-band waves (UB), shown by the blue line, were observed closer to the Earth. Note that electron anisotropy is calculated based on equation (2) in Chen et al. (1999) for each energy channel. The energy-time spectrograms showed enhanced electron energy fluxes (Figure 1g) with predominantly positive electron anisotropy from ~1 keV to 30 keV (Figure 1h), providing favorable conditions for whistler-mode wave generation.

## 3 Survey of whistler-mode waves and electron distributions in the dayside magnetosphere

### 3.1 Statistical distribution of whistler-mode waves and electrons

Our study uses fff wave spectra data from THEMIS A, D and E collected between June 2010 and December 2018. An overview of the occurrence rate distributions for UB and LB whistler-mode waves is shown in Figure 2. The top two rows show the wave distribution relative to the magnetopause ($L_{MP}$-L, denoted as $\Delta L_{MP}$) for the UB (Figures 2a–2c) and LB (Figures 2d–2f), respectively. Since the UB wave amplitude is much weaker than that of LB, we set different amplitude ranges for analysis. Figures 2h–2m show the wave amplitudes in the same format as Figure 2a–2f, but as a function of L-shell. The L-shell is calculated using the IGRF magnetic field model (Alken et al., 2021) for simplicity. The bin size is set to 0.5 MLT × 0.5 L (or $\Delta L_{MP}$). The occurrence rate is calculated as the ratio between the time when whistler waves are recorded within each range and the total time when fff data is available inside the magnetosphere. Figures 2g and 2n show the satellite data collection time. Figures 2a-2f show that the wave distributions in the $\Delta L_{MP}$-MLT coordinate exhibit a diagonal trend; wave occurrences tend to peak at ~6 $\Delta L_{MP}$ near dawn and decrease to less than ~1 $\Delta L_{MP}$ near noon. For larger wave amplitudes, regions with high occurrence rates of LB and UB waves are confined to a narrower L-shell range and are located closer to Earth. Specifically, weak and moderate UB waves (Figure 2a & 2b) extend up to ~2 $\Delta L_{MP}$, while large-amplitude UB waves (Figure 2c) are observed closer to the Earth. However, LB waves typically occur within 1 $\Delta L_{MP}$ of the magnetopause across all amplitude ranges near ~12 MLT (Figures 2d–2f). Their amplitudes and occurrence rates are higher in the prenoon sector (6–12 MLT) compared to the postnoon sector (12–18 MLT) at latitudes within ±18°. It is noteworthy that a few bins with a high occurrence rate of weak LB waves (Figure 2d) near dusk, close to Earth, are likely due to hiss in plumes, as determined by detailed examination of individual events. In the L-MLT coordinate, wave distributions no longer display evident diagonal trends. Nevertheless, the waves still tend to occur at higher L-shells from the dawn to the noon sector, which is consistent with the drift-shell splitting feature of energetic electrons. It is important to note that UB waves are predominantly confined to lower L-shells of ~6–8, whereas LB waves extend to higher L-shells (~7–10).

To select the electron energy channel which is most likely associated with whistler-mode wave generation, we estimate the minimum resonant energy for parallel propagating waves with nonrelativistic electrons:

$$E_{min}^{Cyclotron} = \frac{1}{2} m_e c^2 \frac{f_{ce}^2}{f_{pe}^2} \frac{f_{ce}}{f} \left(1 - \frac{f}{f_{ce}}\right)^3, \tag{5}$$

$$E_{min}^{Landau} = \frac{1}{2} m_e c^2 \frac{f_{ce}^2}{f_{pe}^2} \frac{f}{f_{ce}} \left(\frac{\cos\theta - f/f_{ce}}{\cos^2\theta}\right), \tag{6}$$

where $f_{pe}$ is the plasma frequency, $\theta$ is wave normal angle, $m_e$ is the electron mass, and $c$ is the speed of light. Using statistical results of wave frequency spectra and typical $\frac{f_{pe}}{f_{ce}}$ ratios (Li et al., 2010, 2016), we estimate the characteristic electron energies resonating with waves at various frequencies: ~1.5 keV for cyclotron resonance with UB waves, ~4.5 keV for cyclotron or Landau resonance with waves at 0.5 $f_{ce}$, and ~14 keV for cyclotron resonance with LB waves. It is noteworthy that these values represent the approximate energies, and the actual values could vary depending on the wave frequency, wave normal angle, and $\frac{f_{pe}}{f_{ce}}$ ratio. However, these estimates serve our purpose of evaluating the trend in source electron distributions potentially responsible for the LB and UB wave generation.

An overview of electron anisotropy and omni-directional PSDs at 1.5, 4.5 and 14 keV is shown in Figure 3. Figures 3a–3c indicate that high anisotropy extends from the dawnside, away from the magnetopause, toward the noon sector, moving closer to the magnetopause. Additionally, the high anisotropy for higher-energy electrons is distributed closer to the magnetopause than for lower-energy electrons. This pattern may be explained by pitch angle and energy dependent electron drift path which causes drift shell splitting. As electrons with pitch angles close to 90° drift to larger radial distances from the nightside to the dayside, regions of high anisotropy move closer to the magnetopause from dawn until these electrons are lost to the magnetopause near noon. The electron PSD distributions are also influenced by the loss processes through pitch angle scattering (Figures 3d–3f). The regions of high PSD move radially inward as energy increases, possibly because the lower-energy electrons drift to higher L-shells than higher-energy electrons from the nightside, through dawn, to the dayside, due to the more dominant electric drift. In the L-MLT coordinate (Figures 3g–3i), the high anisotropy region at 1.5 keV is concentrated at L ~6–8, which is consistent with the previous UB wave distributions. At 14 keV, the regions of high anisotropy are distributed at a larger radial distance. PSD distributions as a function of L (Figures 3j–3l) also move closer to Earth as energy increases. Based on the minimum resonance energy calculation discussed above, we evaluate the relationship between 1.5 keV electrons and UB waves, 14 keV electrons and LB waves, as well as 4.5 keV electrons and the features of Landau resonance.

### 3.2 Dependence on solar wind dynamic pressure

For simplicity, we will only present the results in the $L_{MP}$-L coordinate in the following section. To investigate the generation of dayside whistler-mode waves, we present the waves together with the relevant electron distribution, which potentially provides the free energy needed for wave generation.

Figure 4 (from top to bottom) shows UB wave amplitude, electron anisotropy, omni-directional electron PSD at 1.5 keV, and the number of samples under various Dp conditions. UB wave amplitude increases as Dp increases and shifts toward the magnetopause from dawn to noon. The average anisotropy reaches as high as 0.6 under quiet conditions (Figure 4d), increases with Dp, and follows the drift pattern of electrons. PSD generally increases with increasing Dp and remains high over 6–9 MLT. At ~12 MLT, anisotropy significantly increases while PSD remains low as Dp increases. The overlap of high anisotropy and high PSD regions is largely consistent with areas of strong UB wave amplitude, suggesting that whistler-mode wave generation requires both high anisotropy and high PSD of resonating electrons.

Figure 5 shows the same format as Figure 4 but for the LB waves and electron distributions at 14 keV. LB wave amplitude increases with rising Dp and exhibits broader spatial coverage compared to UB waves. Strong LB waves (>30 pT) are primarily distributed before 10 MLT within 5 $\Delta L_{MP}$. The anisotropy distribution follows the electron drift path, extending from dawn to postnoon, and slightly moves toward magnetopause under more compressed conditions. The PSD distribution exhibits a similar diagonal trend to that of LB waves. Strong LB waves are found in regions where high electron anisotropy and high PSD overlap, with this coverage being broader than that for UB waves. The MLT ranges of high PSD and LB waves extend up to the noon sector, while anisotropy extends to later MLTs. This confirms the critical role that the fraction of resonant electrons plays in whistler-mode wave growth.

### 3.3 Dependence on geomagnetic activity

In addition to the solar wind dynamic pressure effect, we also evaluate the effects of substorm injections using the AE index as a proxy. Figure 6 presents the overall wave distribution across different levels of AE index and magnetic latitudes ($\lambda$). Since UB wave amplitude is much weaker than LB and the number of samples during active geomagnetic conditions at high latitudes is limited, we combine UB and LB waves to present the total whistler-mode wave amplitude (integrated over the frequency range of 0.05–0.8 $f_{ce}$). Whistler-mode wave amplitude increases as AE increases, while only the near-equatorial wave distribution (top row) exhibits a diagonal trend. As latitude increases, wave amplitudes near the dawn sector (6–10 MLT) decrease but increase near 12 MLT at a distance near 5 $\Delta L_{MP}$ under all AE conditions. This suggests that dawnside waves are most intense near the equator and become weaker as they propagate to higher latitudes, primarily due to Landau damping. Conversely, dayside waves near noon tend to become stronger as they propagate to higher latitudes, likely due to weaker Landau damping and favorable conditions for continuous wave growth in the compressed geomagnetic field lines.

To investigate the generation mechanism of whistler-mode waves, we first focus on the equatorial region in Figure 7, which follows a format similar to Figures 4 and 5. Since LB waves contribute more to the whistler-mode wave power, we use 14 keV electron distribution to compare with the waves. While equatorial anisotropy of 14 keV electrons does not exhibit a clear dependence on the AE index, PSD significantly increases under more compressed conditions over 6–10 MLT, primarily due to injected electrons from the nightside during enhanced substorm activity. By comparing the distribution patterns, the equatorial region of strong waves is consistent with the region where both electron anisotropy and PSD are strong, creating a favorable condition for whistler-mode wave excitation near the equator.

To evaluate latitudinal dependence, we present the wave and 14 keV electron distributions under active AE conditions in Figure 8. Anisotropy decreases from ~0.6 at the equator (Figure 8d) to ~0.3 at higher latitudes (Figure 8f) over 6–12 MLT, and the electron drift pattern becomes less distinct at higher latitudes. As shown in Figures 8g–8i, the PSD only slightly decreases at higher latitudes.

As discussed earlier, whistler-mode wave intensity increases at noon around $\Delta L_{MP} \sim 5$ at high latitudes. However, in this region, neither anisotropy nor PSD remains high. This suggests that waves at high-latitude regions may originate from the equator and then propagate to higher latitudes, with wave amplitudes potentially being amplified during propagation due to the compressed field line configuration and weak Landau damping (e.g., Bortnik et al., 2007). However, other possibilities cannot be completely ruled out. Whistler-mode waves generated within minimum B pockets can propagate equatorward or poleward (Agapitov et al., 2013; da Silva et al., 2016; Santolík et al., 2003), or remain highly localized after their generation (e.g., Kang et al., 2021).

## 4 Discussion

The overall dawn-dusk asymmetry of whistler-mode wave distribution is consistent with the previous studies using different satellite missions (Agapitov et al., 2013, 2018; Aryan et al., 2014; Bortnik et al., 2007; Meredith et al., 2001, 2014; Sigsbee et al., 2010). Our statistical findings also indicate that positive anisotropy tends to trigger dayside whistler-mode wave generation inside the magnetopause. The anisotropic electron distribution naturally develops from injected electrons originating in the magnetotail, which subsequently drift from the nightside, through dawn, to the dayside, accompanied by drift-shell splitting (Kennel & Petschek, 1966; Ma et al., 2022; Min et al., 2010). This process tends to form the pancake distributions with higher anisotropies observed at higher L-shells (e.g., Li et al., 2010), where geomagnetic fields are more uniform (e.g., Keika et al., 2012). The combination of these two effects may provide favorable locations for whistler-mode wave excitation in the dayside outer magnetosphere.

Since Tsurutani & Smith (1977) proposed the concept of minimum B pockets, many studies have shown strong whistler-mode waves and enhanced electron fluxes at higher latitudes (~20°–40°) in the dayside outer magnetosphere (Antonova & Nikolaeva, 1979; Keika et al., 2012; Spasojavic & Inan, 2010). Although our statistical survey is confined to latitudes within 18° due to the THEMIS orbits, the results support the idea that increasing solar wind pressure can alter the field configuration and enhance the linear and nonlinear growth rates of whistler-mode waves, facilitating phase trapping of electrons inside the wave potential well (Bell & Inan, 1981; Dowden et al., 1978; Fu et al., 2012; Fujiwara et al., 2022; Katoh & Omura, 2013; Nunn, 1974; Omura et al., 1991, Tao et al., 2014; Zhou et al., 2015).

Peng et al. (2020) reported a chorus wave event on the dayside in the magnetosphere, accompanied by solar wind dynamic pressure fluctuations. Their linear wave growth rate calculations indicated that dayside electron flux enhancements driven by increased dynamic pressure provided free energy necessary for chorus wave amplification. However, in another storm-time event, He et al. (2015) showed that the calculated linear growth rate on the dayside was lower than on the nightside due to the lack of a sufficient free energy source, as energetic electron fluxes were lower. Moreover, considering nonlinear wave growth effects, Voshchepynets et al. (2024) used multi-point observations to show that nonlinear growth rates more closely matched measured values compared to linear growth rates, particularly for wave amplification at magnetic latitudes larger than 5°. It is important to note that linear instability is not the sole factor governing wave growth and spectral evolution; nonlinear effects also play a crucial role in the wave growth process (e.g., Omura et al., 2008; Voshchepynets et al., 2014). However, these nonlinear processes are known to initiate with seed waves at frequencies near the maximum linear growth rate (Omura et al., 2008). Therefore, the linear wave growth rate serves as a valuable proxy for estimating the approximate frequency range where positive wave growth is possible.

Despite these findings, additional factors should be considered when examining the high occurrence rates of dayside whistler-mode waves. For example, drift shell bifurcation, a non-adiabatic process (Öztürk & Wolf, 2007; Shabansky, 1971), allows electrons to access the two off-equatorial branches from dawn, where the resonant energies are minimized. Moreover, ULF wave modulation can also impact whistler-mode wave growth (Manninen et al., 2010; Kimura et al., 1974; Spanswick et al., 2005).

## 5 Conclusions

We used eight years of high-resolution data from the THEMIS satellites to statistically evaluate the properties of dayside whistler-mode waves and source electrons, which potentially provide the free energy for wave generation. Since the generation of dayside whistler-mode waves is closely related to the geometry of the Earth's magnetic field lines, we used the new $L_{MP}$-L coordinate to assess these properties, which distinguishes our approach from previous studies. The main findings of our study are summarized below:

1. The occurrence rates of lower-band (LB) and upper-band (UB) waves are higher in regions farther from the magnetopause at dawn and dusk, whereas they are distributed closer to the magnetopause near noon. Additionally, LB waves are observed closer to the magnetopause compared to UB waves.
2. For larger wave amplitudes, regions with high occurrence rates of LB and UB waves are confined to a narrower L-shell range and are located closer to Earth. Their amplitudes and occurrence rates are higher in the prenoon sector (6–12 MLT) compared to the post-noon sector (12–18 MLT) at latitudes within ±18°.
3. When analyzing electron distributions potentially responsible for whistler-mode wave generation, the overall electron phase space density (PSD) at 1.5, 4.5 and 14 keV decreases from 6 to 14 MLT. Additionally, the PSD is higher on the dawn side compared to the dusk side. The distributions of electron anisotropy follow the drift shell splitting pattern, with high anisotropy of a few keV electrons distributed closer to the magnetopause from dawn to noon.
4. The evaluation of the responses of whistler-mode waves and electron distributions under different conditions indicates that wave amplitude, electron anisotropy and PSD increase as dynamic pressure and AE index increase, particularly from the dawn to the afternoon sector. The overlap regions of high anisotropy and high PSD are mostly consistent with areas of strong wave amplitude, with this coverage being broader for LB waves compared to UB waves.
5. Near the equator, wave amplitude and electron PSD increase with a rising AE index, while anisotropy exhibits minimal variation, remaining within the range of ~0.4–0.6. Under disturbed conditions, electron anisotropy decreases from 0.6 to 0.3 with increasing magnetic latitudes in the prenoon sector, whereas whistler-mode wave amplitudes remain steady at 20–30 pT or even slightly increase near noon at ~5 $\Delta L_{MP}$. These features suggest that wave propagation from the equator to higher latitudes, along with amplification along the propagation path, is necessary to explain the observed waves on the dayside.

**Acknowledgments**

We acknowledge the NASA grants 80NSSC25K7686, 80NSSC22K1638, 80NSSC23K0096, 80NSSC24K0239, 80NSSC24K0572, and 80NSSC24K0266, and NSF grants AGS-1847818, AGS-2247774, AGS- 2225445 and AGS-2402179. The authors acknowledge NASA contract NAS5-02099 and V. Angelopoulos for use of data from the THEMIS/ARTEMIS Mission. Specifically, we acknowledge C. W. Carlson and J. P. McFadden for use of ESA data, J. W. Bonnell and F. S. Mozer for use of EFI data, O. LeContel and A. Roux for use of SCM data and K. H. Glassmeier, U. Auster and W. Baumjohann for the use of FGM data.

**Open Research**

The THEMIS data are sourced from the mission website (Angelopoulos, 2007). Solar wind parameters and geomagnetic indices are obtained from the OMNI dataset (Papitashvili et al., 2020). Data used to produce the statistical figures in the present study are available from Peng (2024).

## References

Abel, G. A., Freeman, M. P., Smith, A. J., & Reeves, G. D. (2006). Association of substorm chorus events with Drift Echoes. *Journal of Geophysical Research*, *111*(A11). https://doi.org/10.1029/2006ja011860

Agapitov, O., Krasnoselskikh, V., Zaliznyak, Yu., Angelopoulos, V., Le Contel, O., and Rolland, G. (2011). Observations and modeling of forward and reflected chorus waves captured by THEMIS, Ann. Geophys., 29, 541–550, https://doi.org/10.5194/angeo-29-541-2011.

Agapitov, O., Krasnoselskikh, V., Khotyaintsev, Y. V., & Rolland, G. (2012). Correction to "A statistical study of the propagation characteristics of whistler waves observed by Cluster." *Geophysical Research Letters*, *39*(24). https://doi.org/10.1029/2012gl054320

Agapitov, O., A. Artemyev, V. Krasnoselskikh, Y. V. Khotyaintsev, D. Mourenas, H. Breuillard, M. Balikhin, and G. Rolland (2013), Statistics of whistler-mode waves in the outer radiation belt: Cluster STAFF-SA measurements, *J. Geophys. Res. Space Physics*, 118, 3407–3420, doi:10.1002/jgra.50312.

Agapitov, O. V., Mourenas, D., Artemyev, A. V., Mozer, F. S., Hospodarsky, G., Bonnell, J., & Krasnoselskikh, V. (2018). Synthetic empirical chorus wave model from combined Van Allen Probes and Cluster statistics. Journal of Geophysical Research: Space Physics, 123, 297–314. https://doi.org/10.1002/2017JA024843

Albert, J. M. (2000). Gyroresonant interactions of radiation belt particles with a monochromatic electromagnetic wave. *Journal of Geophysical Research: Space Physics*, *105*(A9), 21191–21209. https://doi.org/10.1029/2000ja000008

Alken, P., Thébault, E., Beggan, C.D. et al. (2021), International Geomagnetic Reference Field: the thirteenth generation, Earth Planets Space 73, 49, doi: 10.1186/s40623-020-01288-x.

Angelopoulos, V. (2007). THEMIS data [Dataset]. University of California. Retrieved from https://themis.ssl.berkeley.edu/data/themis/.

Angelopoulos, V. (2008). The Themis Mission. *Space Science Reviews*, *141*(1–4), 5–34. https://doi.org/10.1007/s11214-008-9336-1.

Angelopoulos, V. The ARTEMIS Mission. Space Sci Rev 165, 3–25 (2011). https://doi.org/10.1007/s11214-010-9687-2

Antonova, A. E., & Nikolaeva, N. S. (1979). On localization of energetic electrons in the outer magnetosphere of the earth. Geomagnetism and Aeronomy, 19, 802–805.

Aryan, H., Yearby, K., Balikhin, M., Agapitov, O., Krasnoselskikh, V., & Boynton, R. (2014). Statistical study of chorus wave distributions in the inner magnetosphere using *Ae* and solar wind parameters. *Journal of Geophysical Research: Space Physics*, *119*(8), 6131–6144. https://doi.org/10.1002/2014ja019939

Auster, H. U., Glassmeier, K. H., Magnes, W., Aydogar, O., Baumjohann, W., Constantinescu, D., Fischer, D., Fornacon, K. H., Georgescu, E., Harvey, P., Hillenmaier, O., Kroth, R., Ludlam, M., Narita, Y., Nakamura, R., Okrafka, K., Plaschke, F., Richter, I., Schwarzl, H., … Wiedemann, M. (2008). The Themis Fluxgate magnetometer. *Space Science Reviews*, *141*(1–4), 235–264. https://doi.org/10.1007/s11214-008-9365-9

Bell, T. F., & Inan, U. S. (1981). Transient nonlinear pitch angle scattering of energetic electrons by coherent VLF wave packets in the magnetosphere. *Journal of Geophysical Research*, *86*(A11), 9047. https://doi.org/10.1029/ja086ia11p09047

Breuillard, H., Zaliznyak, Y., Agapitov, O., Artemyev, A., Krasnoselskikh, V., and Rolland, G. (2013). Spatial spreading of magnetospherically reflected chorus elements in the inner magnetosphere, Ann. Geophys., 31, 1429–1435, https://doi.org/10.5194/angeo-31-1429-2013.

Bortnik, J., U. S. Inan, and T. F. Bell (2006), Landau damping and resultant unidirectional propagation of chorus waves, Geophys. Res. Lett., 33, L03102, doi:10.1029/2005GL024553.

Bortnik, J., Thorne, R. M., & Meredith, N. P. (2007). Modeling the propagation characteristics of chorus using CRRES suprathermal electron fluxes. *Journal of Geophysical Research: Space Physics*, *112*(A8). https://doi.org/10.1029/2006ja012237.

Bortnik, J., Thorne, R. M., & Inan, U. S. (2008). Nonlinear interaction of energetic electrons with large amplitude chorus. *Geophysical Research Letters*, *35*(21). https://doi.org/10.1029/2008gl035500.

Bortnik, J., W. Li, R. M. Thorne, V. Angelopoulos, C. Cully, J. Bonnell, O. Le Contel, and A. Roux (2009), An observation linking the origin of plasmaspheric hiss to discrete chorus emissions, *Science*, **324**, 775, doi:10.1126/science.1171273.

Bortnik, J., L. Chen, W. Li, R. M. Thorne, N. P. Meredith, and R. B. Horne (2011), Modeling the wave power distribution and characteristics of plasmaspheric hiss, *J. Geophys. Res.*, **116**, A12209, doi:10.1029/2011JA016862.

Burtis, W. J., & Helliwell, R. A. (1969). Banded chorus-a new type of VLF radiation observed in the magnetosphere by Ogo 1 and Ogo 3. *Journal of Geophysical Research*, *74*(11), 3002–3010. https://doi.org/10.1029/ja074i011p03002

Burton, R. K., & Holzer, R. E. (1974). The origin and propagation of chorus in the outer magnetosphere. *Journal of Geophysical Research*, *79*(7), 1014–1023. https://doi.org/10.1029/ja079i007p01014

Chen L., R. M. Thorne, W. Li, and J. Bortnik (2013), Modeling the wave normal distribution of chorus waves, *J. Geophys. Res. Space Physics*, 118, 1074–1088, doi:10.1029/2012JA018343.

Chen, M. W., Roeder, J. L., Fennell, J. F., Lyons, L. R., Lambour, R. L., & Schulz, M. (1999). Proton ring current pitch angle distributions: Comparison of simulations with CRRES observations. *Journal of Geophysical Research: Space Physics*, *104*(A8), 17379–17389. https://doi.org/10.1029/1999ja900142

Chen, Y., G. D. Reeves, and R. H. W. Friedel (2007), The energization of relativistic electrons in the outer Van Allen radiation belt, Nat. Phys., 3, 614–617, doi:10.1038/nphys655.

Chen, L., Bortnik, J., Li, W., Thorne, R. M., & Horne, R. B. (2012a). Modeling the properties of plasmaspheric hiss: 1. Dependence on chorus wave emission. *Journal of Geophysical Research*, **117**, A05201. https://doi.org/10.1029/2011JA017201

Chen, L., Bortnik, J., Li, W., Thorne, R. M., & Horne, R. B. (2012b). Modeling the properties of plasmaspheric hiss: 2. Dependence on the plasma density distribution. *Journal of Geophysical Research*, **117**, A05202. https://doi.org/10.1029/2011JA017202

Chum, J., & Santolík, O. (2005). Propagation of whistler-mode chorus to low altitudes: Divergent Ray trajectories and Ground Accessibility. *Annales Geophysicae*, *23*(12), 3727–3738. https://doi.org/10.5194/angeo-23-3727-2005

Church, S. R., and R. M. Thorne (1983), On the origin of plasmaspheric hiss: Ray path integrated amplification, J. Geophys. Res., 88(A10), 7941–7957, doi:10.1029/JA088iA10p07941.

Colpitts, C., Miyoshi, Y., Kasahara, Y., Delzanno, G. L., Wygant, J. R., Cattell, C. A., et al. (2020). First direct observations of propagation of discrete chorus elements from the equatorial source to higher latitudes, using the Van Allen Probes and Arase satellites. *Journal of Geophysical Research: Space Physics*, 125, e2020JA028315. https://doi.org/10.1029/2020JA028315

Cully, C. M., Ergun, R. E., Stevens, K., Nammari, A., & Westfall, J. (2008). The Themis Digital Fields Board. *Space Science Reviews*, *141*(1–4), 343–355. https://doi.org/10.1007/s11214-008-9417-1

da Silva, C. L., Wu, S., Denton, R. E., Hudson, M. K., & Millan, R. M. (2017). Hybrid fluid-particle simulation of whistler-mode waves in a compressed dipole magnetic field: Implications for Dayside high-latitude chorus. *Journal of Geophysical Research: Space Physics*, *122*(1), 432–448. https://doi.org/10.1002/2016ja023446

Dowden, R. L., McKay, A. D., Amon, L. E., Koons, H. C., & Dazey, M. H. (1978). Linear and nonlinear amplification in the magnetosphere during a 6.6-KHz transmission. *Journal of Geophysical Research: Space Physics*, *83*(A1), 169–181. https://doi.org/10.1029/ja083ia01p00169

Draganov, A. B., Inan, U. S., Sonwalkar, V. S., & Bell, T. F. (1992). Magnetospherically reflected whistlers as a source of plasmaspheric hiss. *Geophysical Research Letters*, **19**, 233–236. https://doi.org/10.1029/91GL03167

Fu, H. S., J. B. Cao, F. S. Mozer, H. Y. Lu, and B. Yang (2012), Chorus intensification in response to interplanetary shock, J. Geophys. Res., 117, A01203, doi:10.1029/2011JA016913.

Fujiwara, Y., Nogi, T. & Omura, Y. Nonlinear triggering process of whistler-mode emissions in a homogeneous magnetic field. *Earth Planets Space* **74**, 95 (2022). https://doi.org/10.1186/s40623-022-01646-x

Gan, L., Li, W., Ma, Q., Albert, J. M., Artemyev, A. V., & Bortnik, J. (2020). Nonlinear interactions between radiation belt electrons and chorus waves: Dependence on wave amplitude modulation. *Geophysical Research Letters*, *47*(4). https://doi.org/10.1029/2019gl085987

Gao, X., Lu, Q., Bortnik, J., Li, W., Chen, L., & Wang, S. (2016). Generation of multiband chorus by lower band cascade in the Earth's magnetosphere. *Geophysical Research Letters*, *43*(6), 2343–2350. https://doi.org/10.1002/2016gl068313

Green, J. L., S. Boardsen, L. Garcia, W. W. L. Taylor, S. F. Fung, and B. W. Reinisch (2005), On the origin of whistler mode radiation in the plasmasphere, J. Geophys. Res., 110, A03201, doi:10.1029/2004JA010495.

Haaland, S., Runov, A., Artemyev, A., & Angelopoulos, V. (2019). Characteristics of the flank magnetopause: THEMIS observations. *Journal of Geophysical Research: Space Physics*, 124, 3421–3435. https://doi.org/10.1029/2019JA026459

Hayakawa, M., Yamanaka, Y., Parrot, M., & Lefeuvre, F. (1984). The Wave Normals of magnetospheric chorus emissions observed on board GEOS 2. *Journal of Geophysical Research*, *89*(A5), 2811. https://doi.org/10.1029/ja089ia05p02811

He, Y., Xiao, F., Zhou, Q., Yang, C., Liu, S., Baker, D. N., Kletzing, C. A., Kurth, W. S., Hospodarsky, G. B., Spence, H. E., Reeves, G. D., Funsten, H. O., & Blake, J. B. (2015). Van allen probes observation and modeling of chorus excitation and propagation during weak geomagnetic activities. *Journal of Geophysical Research: Space Physics*, *120*(8), 6371–6385. https://doi.org/10.1002/2015ja021376

Horne, R. B., & Thorne, R. M. (2003). Relativistic electron acceleration and precipitation during resonant interactions with Whistler-Mode Chorus. *Geophysical Research Letters*, *30*(10). https://doi.org/10.1029/2003gl016973

Horne, Richard B., Thorne, R. M., Shprits, Y. Y., Meredith, N. P., Glauert, S. A., Smith, A. J., Kanekal, S. G., Baker, D. N., Engebretson, M. J., Posch, J. L., Spasojevic, M., Inan, U. S., Pickett, J. S., & Decreau, P. M. (2005). Wave acceleration of electrons in the Van Allen Radiation Belts. *Nature*, *437*(7056), 227–230. https://doi.org/10.1038/nature03939

Kang, N., Bortnik, J., An, X., & Claudepierre, S. G. (2021). Propagation of chorus waves generated in minimum-b pockets. *Geophysical Research Letters*, *48*(24). https://doi.org/10.1029/2021gl096478

Katoh, Y., & Omura, Y. (2013). Effect of the background magnetic field inhomogeneity on generation processes of Whistler-mode chorus and broadband hiss-like emissions. *Journal of Geophysical Research: Space Physics*, *118*(7), 4189–4198. https://doi.org/10.1002/jgra.50395

Keika, K., Spasojevic, M., Li, W., Bortnik, J., Miyoshi, Y., & Angelopoulos, V. (2012). Penguin/Ago and Themis conjugate observations of Whistler Mode Chorus waves in the Dayside uniform zone under steady solar wind and quiet geomagnetic conditions. *Journal of Geophysical Research: Space Physics*, *117*(A7). https://doi.org/10.1029/2012ja017708

Kennel, C. F., & Petschek, H. E. (1966). Limit on stably trapped particle fluxes. *Journal of Geophysical Research*, *71*(1), 1–28. https://doi.org/10.1029/jz071i001p00001

Kimura, I. (1974), Interrelation between VLF and ULF emissions, Space Sci. Rev., 16, 389–411, doi:10.1007/BF00171565.

Koons, H. C., & Roeder, J. L. (1990). A survey of equatorial magnetospheric wave activity between 5 and 8 re. *Planetary and Space Science*, *38*(10), 1335–1341. https://doi.org/10.1016/0032-0633(90)90136-e

Lauben, D. S., Inan, U. S., Bell, T. F., & Gurnett, D. A. (2002). Source characteristics of Elf/VLF Chorus. *Journal of Geophysical Research: Space Physics*, *107*(A12). https://doi.org/10.1029/2000ja003019

LeDocq, M. J., Gurnett, D. A., & Hospodarsky, G. B. (1998). Chorus source locations from VLF Poynting flux measurements with the Polar Spacecraft. *Geophysical Research Letters*, *25*(21), 4063–4066. https://doi.org/10.1029/1998gl900071

Li, J., Bortnik, J., An, X. et al. Origin of two-band chorus in the radiation belt of Earth. Nat Commun 10, 4672 (2019). https://doi.org/10.1038/s41467-019-12561-3.

Li, W., Shprits, Y. Y., & Thorne, R. M. (2007). Dynamic evolution of energetic outer zone electrons due to wave-particle interactions during storms. *Journal of Geophysical Research: Space Physics*, *112*(A10). https://doi.org/10.1029/2007ja012368

Li, W., R. M. Thorne, N. P. Meredith, R. B. Horne, J. Bortnik, Y. Y. Shprits, and B. Ni (2008), Evaluation of whistler mode chorus amplification during an injection event observed on CRRES, J. Geophys. Res., 113, A09210, doi:10.1029/2008JA013129.

Li, W., Thorne, R. M., Angelopoulos, V., Bortnik, J., Cully, C. M., Ni, B., LeContel, O., Roux, A., Auster, U., & Magnes, W. (2009). Global distribution of whistler-mode chorus waves observed on the Themis spacecraft. *Geophysical Research Letters*, *36*(9). https://doi.org/10.1029/2009gl037595

Li, W., Thorne, R. M., Nishimura, Y., Bortnik, J., Angelopoulos, V., McFadden, J. P., Larson, D. E., Bonnell, J. W., Le Contel, O., Roux, A., & Auster, U. (2010). Themis analysis of observed equatorial electron distributions responsible for the chorus excitation. *Journal of Geophysical Research: Space Physics*, *115*(A6). https://doi.org/10.1029/2009ja014845

Li, W., Bortnik, J., Thorne, R. M., Cully, C. M., Chen, L., Angelopoulos, V., Nishimura, Y., Tao, J. B., Bonnell, J. W., & LeContel, O. (2013). Characteristics of the Poynting flux and wave normal vectors of whistler-mode waves observed on Themis. *Journal of Geophysical Research: Space Physics*, *118*(4), 1461–1471. https://doi.org/10.1002/jgra.50176.

Li, W., Santolik, O., Bortnik, J., Thorne, R. M., Kletzing, C. A., Kurth, W. S., and Hospodarsky, G. B. (2016), New chorus wave properties near the equator from Van Allen Probes wave observations, Geophys. Res. Lett., 43, 4725–4735, doi:10.1002/2016GL068780.

Liu, K., Gary, S. P., & Winske, D. (2011). Excitation of banded whistler waves in the magnetosphere. *Geophysical Research Letters*, *38*(14). https://doi.org/10.1029/2011gl048375

Lorentzen, K. R., Blake, J. B., Inan, U. S., & Bortnik, J. (2001). Observations of relativistic electron microbursts in association with VLF Chorus. *Journal of Geophysical Research: Space Physics*, *106*(A4), 6017–6027. https://doi.org/10.1029/2000ja003018

Ma, J., Gao, X., Chen, H., Tsurutani, B. T., Ke, Y., Chen, R., & Lu, Q. (2022). The effects of substorm injection of energetic electrons and enhanced solar wind ram pressure on whistler-mode chorus waves: A statistical study. *Journal of Geophysical Research: Space Physics*, 127, e2022JA030502. https://doi.org/10.1029/2022JA030502

Manninen, J., N. G. Kleimenova, O. V. Kozyreva, and T. Turunen (2010), Pc5 geomagnetic pulsations, pulsating particle precipitation, and VLF chorus: Case study on 24 November 2006, J. Geophys. Res., 115, A00F14, doi:10.1029/2009JA014837.

McFadden, J. P., Carlson, C. W., Larson, D., Ludlam, M., Abiad, R., Elliott, B., Turin, P., Marckwordt, M., & Angelopoulos, V. (2008). The THEMIS ESA plasma instrument and in-flight calibration. *Space Science Reviews*, *141*(1–4), 277–302. https://doi.org/10.1007/s11214-008-9440-2

Meredith, N. P., Horne, R. B., & Anderson, R. R. (2001). Substorm dependence of chorus amplitudes: Implications for the acceleration of electrons to relativistic energies. *Journal of Geophysical Research: Space Physics*, *106*(A7), 13165–13178. https://doi.org/10.1029/2000ja900156

Meredith, N. P., R. B. Horne, R. M. Thorne, D. Summers, and R. R. Anderson (2004), Substorm dependence of plasmaspheric hiss, *J. Geophys. Res.*, **109**, A06209, doi:10.1029/2004JA010387.

Meredith, N. P., R. B. Horne, M. A. Clilverd, D. Horsfall, R. M. Thorne, and R. R. Anderson (2006), Origins of plasmaspheric hiss, *J. Geophys. Res.*, **111**, A09217, doi:10.1029/2006JA011707.1

Meredith, N. P., R. B. Horne, A. Sicard-Piet, D. Boscher, K. H. Yearby, W. Li, and R. M. Thorne (2012), Global model of lower band and upper band chorus from multiple satellite observations, J. Geophys. Res., 117, A10225, doi:10.1029/2012JA017978.

Meredith, N. P., R. B. Horne, W. Li, R. M. Thorne, and A. Sicard-Piet (2014), Global model of low-frequency chorus ($f_{LHR}<f<0.1f_{ce}$) from multiple satellite observations, *Geophys. Res. Lett.*, 41, 280–286, doi:10.1002/2013GL059050.

Min, K., J. Lee, and K. Keika (2010), Chorus wave generation near the dawnside magnetopause due to drift shell splitting of substorm-injected electrons, *J. Geophys. Res.*, 115, A00I02, doi:10.1029/2010JA015474.

Nishimura, Y., Bortnik, J., Li, W., Thorne, R. M., Lyons, L. R., Angelopoulos, V., Mende, S. B., Bonnell, J. W., Le Contel, O., Cully, C., Ergun, R., & Auster, U. (2010). Identifying the driver of pulsating Aurora. *Science*, *330*(6000), 81–84. https://doi.org/10.1126/science.1193186

Nunn, D. (1974). A self-consistent theory of triggered VLF emissions. *Planetary and Space Science*, *22*(3), 349–378. https://doi.org/10.1016/0032-0633(74)90070-1

Omura, Y., Nunn, D., Matsumoto, H., & Rycroft, M. J. (1991). A review of observational, theoretical and numerical studies of VLF triggered emissions. *Journal of Atmospheric and Terrestrial Physics*, *53*(5), 351–368. https://doi.org/10.1016/0021-9169(91)90031-2

Omura, Y., Y. Katoh, and D. Summers (2008), Theory and simulation of the generation of whistler-mode chorus, J. Geophys. Res., 113, A04223, doi:10.1029/2007JA012622.

O'Brien, T. P. (2004). Quantification of relativistic electron microburst losses during the gem storms. *Geophysical Research Letters*, *31*(4). https://doi.org/10.1029/2003gl018621

Öztürk, M. K., & Wolf, R. A. (2007). Bifurcation of drift shells near the dayside magnetopause. *Journal of Geophysical Research: Space Physics*, *112*(A7). https://doi.org/10.1029/2006ja012102

Papitashvili, Natalia E. and King, Joseph H. (2020), "OMNI 1-min Data", https://omniweb.gsfc.nasa.gov/

Peng, Q., Li, H., Tang, R., Zhong, Z., Zhang, H., & Li, Q. (2020). Variation of dayside chorus waves associated with solar wind dynamic pressure based on MMS observations. *Advances in Space Research*, *65*(11), 2551–2558. https://doi.org/10.1016/j.asr.2020.03.006

Peng, Y. (2024). Data used to produce figures in the present paper entitled "Statistical Properties and Distributions of Dayside Whistler-mode Waves Under Various Solar Wind Conditions" [Dataset]. Retrieved from https://doi.org/10.5281/zenodo.13375938.

Pickett, J. S., Franz, J. R., Scudder, J. D., Menietti, J. D., Gurnett, D. A., Hospodarsky, G. B., Braunger, R. M., Kintner, P. M., & Kŭrth, W. S. (2001). Plasma waves observed in the cusp turbulent boundary layer: An analysis of high time resolution wave and particle measurements from the Polar spacecraft. *Journal of Geophysical Research: Space Physics*, *106*(A9), 19081–19099. https://doi.org/10.1029/2000ja003012

Santolík, O. (2003). Spatio-temporal structure of storm-time chorus. *Journal of Geophysical Research*, *108*(A7). https://doi.org/10.1029/2002ja009791

Santolík, O., Macúšová, E., Yearby, K. H., Cornilleau-Wehrlin, N., & Alleyne, H. StC. (2005). Radial variation of Whistler-Mode Chorus: First Results from the staff/DWP instrument on board the Double Star TC-1 spacecraft. *Annales Geophysicae*, *23*(8), 2937–2942. https://doi.org/10.5194/angeo-23-2937-2005

Santolík, O., E. Macúšová, I. Kolmašová, N. Cornilleau-Wehrlin, and Y. de Conchy (2014), Propagation of lower-band whistler-mode waves in the outer Van Allen belt: Systematic analysis of 11 years of multi-component data from the Cluster spacecraft, *Geophys. Res. Lett.*, 41, 2729–2737, doi:10.1002/2014GL059815.

Schriver, D., Ashour-Abdalla, M., Coroniti, F. V., LeBoeuf, J. N., Decyk, V., Travnicek, P., Santolík, O., Winningham, D., Pickett, J. S., Goldstein, M. L., & Fazakerley, A. N. (2010). Generation of Whistler mode emissions in the Inner Magnetosphere: An Event Study. *Journal of Geophysical Research: Space Physics*, *115*(A8). https://doi.org/10.1029/2009ja014932

Shabansky, V. P. (1971). Some processes in the magnetosphere. *Space Science Reviews*, *12*(3), 299–418. https://doi.org/10.1007/bf00165511

Shi, R., Li, W., Ma, Q., Claudepierre, S. G., Kletzing, C. A., Kurth, W. S., Hospodarsky, G. B., Spence, H. E., Reeves, G. D., Fennell, J. F., Blake, J. B., Thaller, S. A., & Wygant, J. R. (2018). Van Allen Probes observation of plasmaspheric hiss modulated by injected energetic electrons. *Annales de Geophysique*, **36**, 781–791. https://doi.org/10.5194/angeo-36-781-2018

Shue, J.-H., Chao, J. K., Fu, H. C., Russell, C. T., Song, P., Khurana, K. K., & Singer, H. J. (1997). A new functional form to study the solar wind control of the magnetopause size and shape. *Journal of Geophysical Research: Space Physics*, *102*(A5), 9497–9511. https://doi.org/10.1029/97ja00196

Sigsbee, K., Menietti, J. D., Santolík, O., & Pickett, J. S. (2010). Locations of chorus emissions observed by the Polar Plasma Wave Instrument. *Journal of Geophysical Research: Space Physics*, *115*(A6). https://doi.org/10.1029/2009ja014579

Smith, A. J., Freeman, M. P., Wickett, M. G., & Cox, B. D. (1999). On the relationship between the magnetic and VLF signatures of the substorm expansion phase. *Journal of Geophysical Research: Space Physics*, *104*(A6), 12351–12360. https://doi.org/10.1029/1998ja900184

Solomon, J., N. Cornilleau-Wehrlin, A. Korth, and G. Kremser (1988), An experimental study of ELF/VLF hiss generation in the Earth's magnetosphere, *J. Geophys. Res.*, 93(A3), 1839–1847, doi:10.1029/JA093iA03p01839.

Spanswick, E., E. Donovan, and G. Baker (2005), Pc5 modulation of high energy electron precipitation: Particle interaction regions and scattering efficiency, Ann. Geophys., 23, 1533–1542, doi:10.5194/angeo-23-15332005.

Spasojevic, M., & Inan, U. S. (2010). Drivers of chorus in the outer dayside magnetosphere. *Journal of Geophysical Research: Space Physics*, *115*(A4). https://doi.org/10.1029/2009ja014452

Stix, T. H., & Scott, F. R. (1963). The theory of Plasma Waves. *American Journal of Physics*, *31*(10), 816–816. https://doi.org/10.1119/1.1969127

Tao, X., Lu, Q., Wang, S., & Dai, L. (2014). Effects of magnetic field configuration on the day-night asymmetry of chorus occurrence rate: A numerical study. *Geophysical Research Letters*, *41*(19), 6577–6582. https://doi.org/10.1002/2014gl061493

Thorne, R. M., E. J. Smith, R. K. Burton, and R. E. Holzer (1973), Plasmaspheric hiss, J. Geophys. Res., 78(10), 1581–1596, doi:10.1029/ JA078i010p01581.

Thorne, R., S. Church, and D. Gorney (1979), On the origin of plasmaspheric hiss: The importance of wave propagation and the plasmapause, *J. Geophys. Res.*, **84**(A9), 5241–5247, doi:10.1029/JA084iA09p05241.

Thorne, R. M., Church, S. R., Malloy, W. J., & Tsurutani, B. T. (1977). The local time variation of elf emissions during periods of substorm activity. *Journal of Geophysical Research*, *82*(10), 1585–1590. https://doi.org/10.1029/ja082i010p01585

Thorne, R. M., Li, W., Ni, B., Ma, Q., Bortnik, J., Chen, L., Baker, D. N., Spence, H. E., Reeves, G. D., Henderson, M. G., Kletzing, C. A., Kurth, W. S., Hospodarsky, G. B., Blake, J. B., Fennell, J. F., Claudepierre, S. G., & Kanekal, S. G. (2013). Rapid local acceleration of relativistic radiation-belt electrons by magnetospheric chorus. *Nature*, *504*(7480), 411–414. https://doi.org/10.1038/nature12889

Thorne, Richard M., Ni, B., Tao, X., Horne, R. B., & Meredith, N. P. (2010). Scattering by chorus waves as the dominant cause of diffuse auroral precipitation. *Nature*, *467*(7318), 943–946. https://doi.org/10.1038/nature09467

Tsurutani, B. T., & Smith, E. J. (1977). Two types of magnetospheric elf chorus and their substorm dependences. *Journal of Geophysical Research*, *82*(32), 5112–5128. https://doi.org/10.1029/ja082i032p05112

Vaivads, A., Santolík, O., Stenberg, G., André, M., Owen, C. J., Canu, P., & Dunlop, M. (2007). Source of Whistler emissions at the Dayside magnetopause. *Geophysical Research Letters*, *34*(9). https://doi.org/10.1029/2006gl029195

Voshchepynets, A., Agapitov, O. V., Mourenas, D., Artemyev, A., Hlebena, M., & Bryla, A. (2024). Latitudinal mapping of chorus waves growth rates based on multi-spacecraft wave and plasma measurements. Geophysical Research Letters, 51, e2024GL110539. https://doi.org/10.1029/2024GL110539

Zhang, X. -J., Thorne, R., Artemyev, A., Mourenas, D., Angelopoulos, V., Bortnik, J., Kletzing, C. A., Kurth, W. S., & Hospodarsky, G. B. (2018). Properties of intense field-aligned lower-band chorus waves: Implications for nonlinear wave-Particle Interactions. *Journal of Geophysical Research: Space Physics*, *123*(7), 5379–5393. https://doi.org/10.1029/2018ja025390

Zhang, X.-J., Mourenas, D., Artemyev, A. V., Angelopoulos, V., Kurth, W. S., Kletzing, C. A., & Hospodarsky, G. B. (2020). Rapid frequency variations within intense chorus wave packets. Geophysical Research Letters, 47, e2020GL088853. https://doi.org/10.1029/2020GL088853

Zhou, C., W. Li, R. M. Thorne, J. Bortnik, Q. Ma, X. An, X.-j. Zhang, V. Angelopoulos, B. Ni, X. Gu, et al. (2015), Excitation of dayside chorus waves due to magnetic field line compression in response to interplanetary shocks, J. Geophys. Res. Space Physics, 120, 8327–8338, doi:10.1002/2015JA021530.

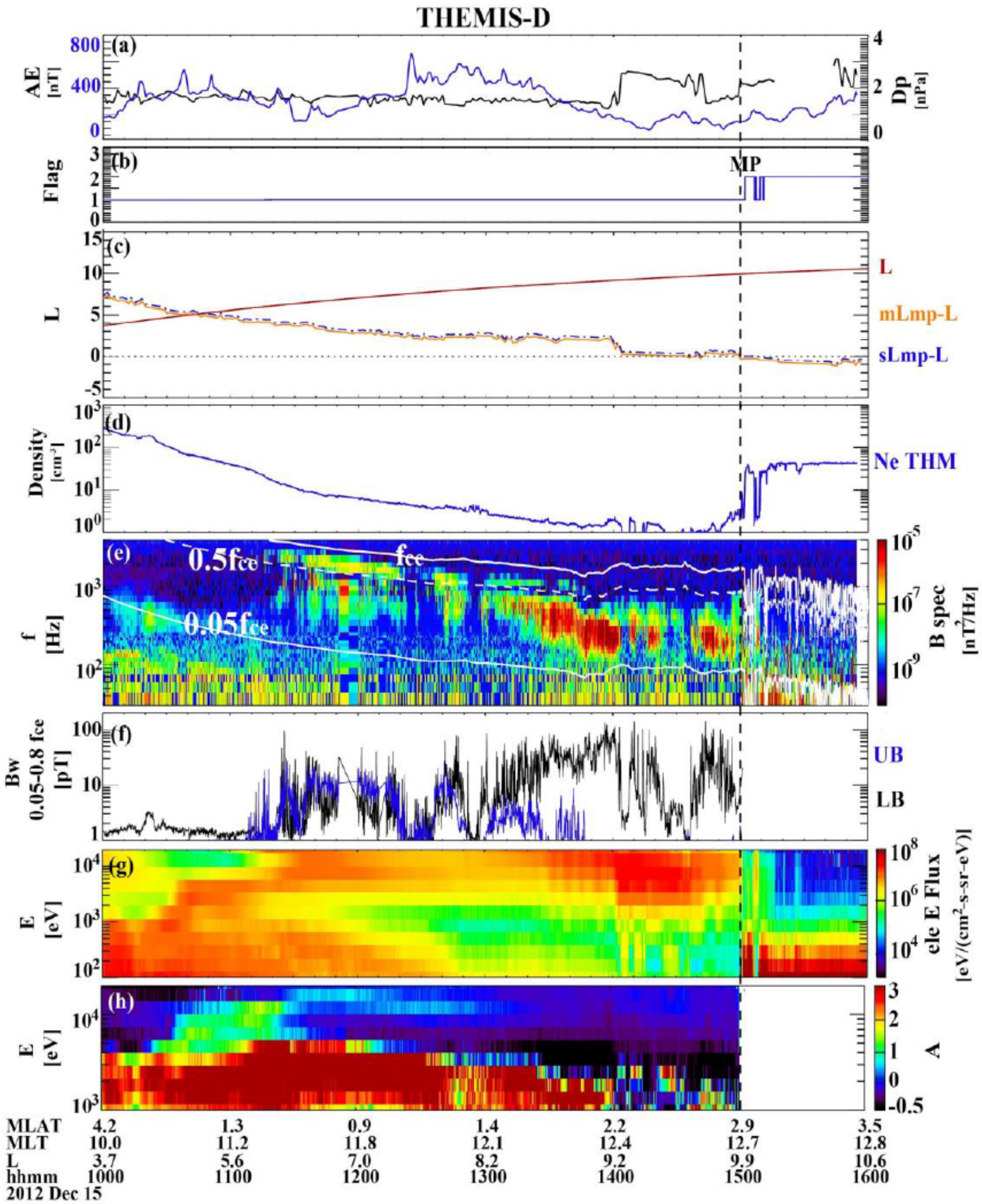


**Figure 1**. Overview of whistler-mode waves observed by THEMIS-D during 10–16 UT on 15 December 2012. (a) AE index in blue and solar wind dynamic pressure (Dp) in black; (b) flag for inside (1) or outside (2) the magnetopause; (c) L-shell (red solid line), modeled distance to the magnetopause $mL_{MP}$-L (orange solid line), and scaled distance to the magnetopause $sL_{MP}$-L (blue dashed line); (d) total electron density inferred from the spacecraft potential; (e) wave magnetic power spectral density with different fractions of electron cyclotron frequency as white lines; (f) upper-band (blue) and lower-band (black) whistler-mode wave amplitudes; (g) energy spectrogram of omni-directional electron energy flux; and (h) electron anisotropy.

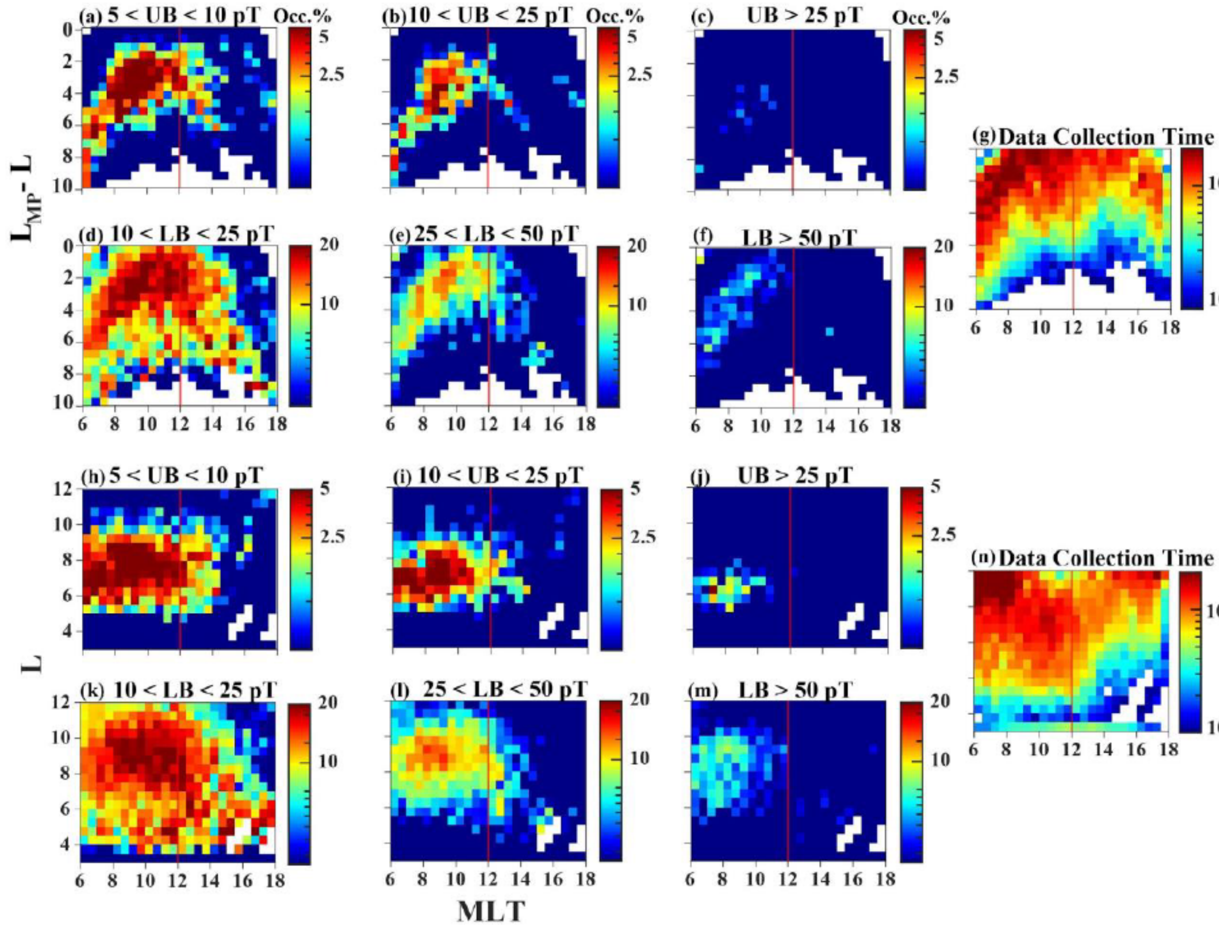


**Figure 2.** Occurrence rate of whistler-mode waves at various MLTs and L-shells. (a)–(c) Occurrence rate of UB, and (d–f) LB whistler-mode waves with different amplitude levels as functions of MLT and $L_{MP}$-L. (h–m) The same format as panels (a–f), but in the L-shell coordinate. (g) Number of samples as functions of MLT and $L_{mp}$-L; (n) Number of samples as functions of MLT and L.

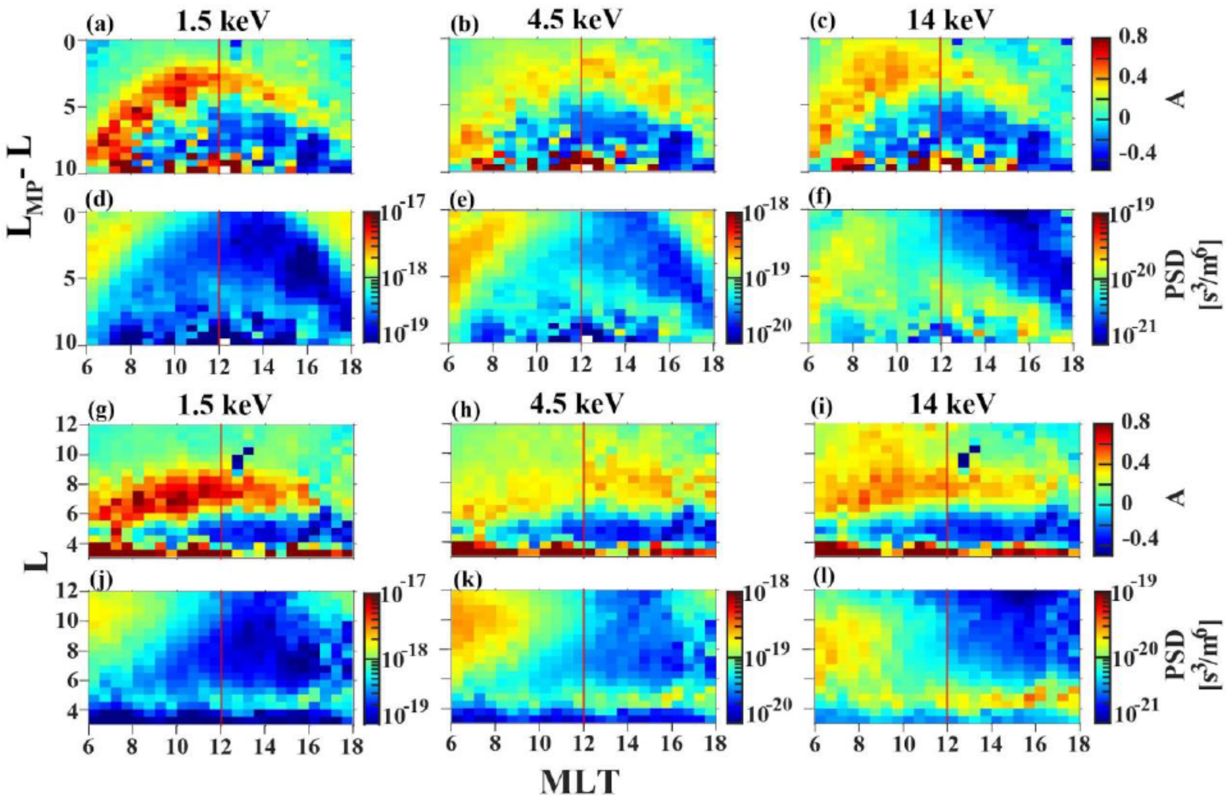


**Figure 3**. Electron anisotropy and omni-directional electron PSD distribution. (a)–(c) Electron anisotropy at 1.5 keV, 4.5 keV, and 14 keV as functions of MLT and $L_{MP}$-L; (d)–(f) Same format as panels (a)–(c), but for omni-directional electron PSD. (g)–(l) Same format as panels (a)–(f), but in the L-shell coordinate.

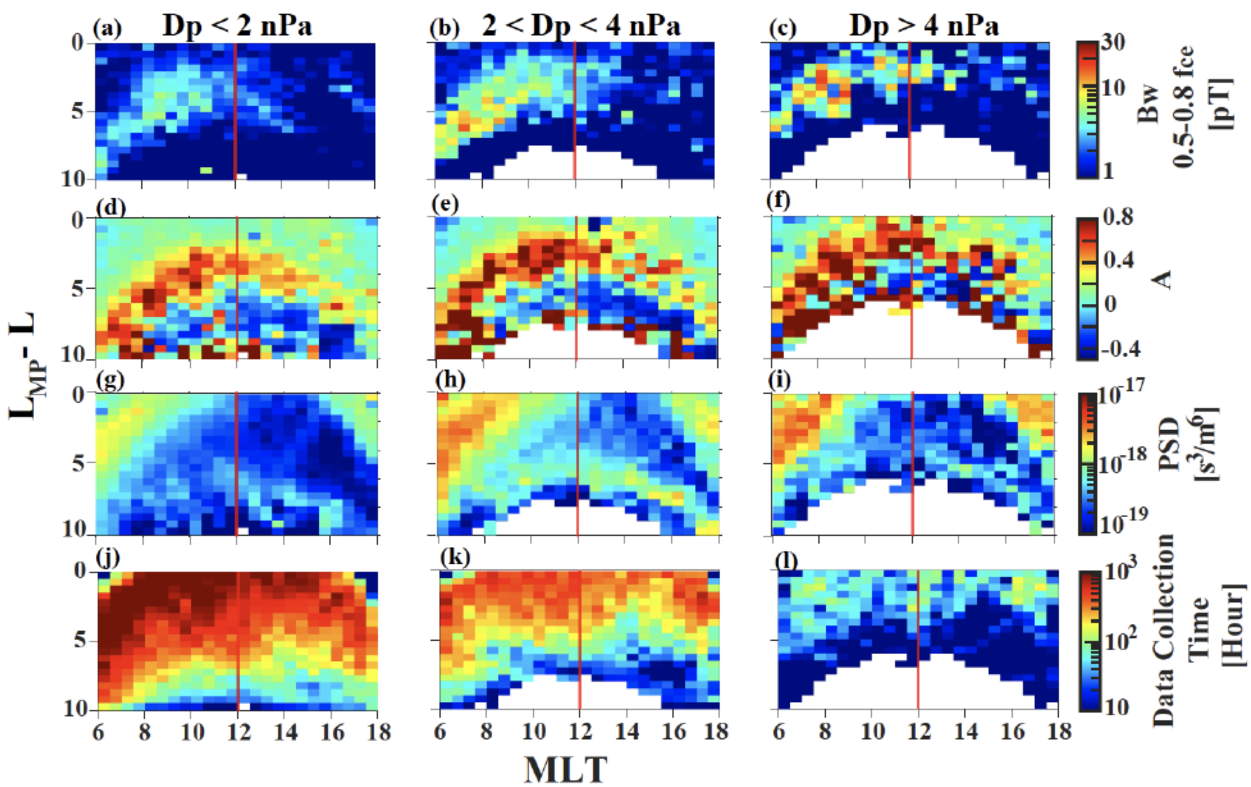


**Figure 4.** Distributions of UB wave amplitude and 1.5 keV electrons as functions of MLT and $L_{MP}$-L. (a–c) UB wave amplitudes; (d–f) electron anisotropy; (g–i) omni-directional electron PSD at 1.5 keV; and (j–l) number of samples in hours under different levels of solar wind dynamic pressure.

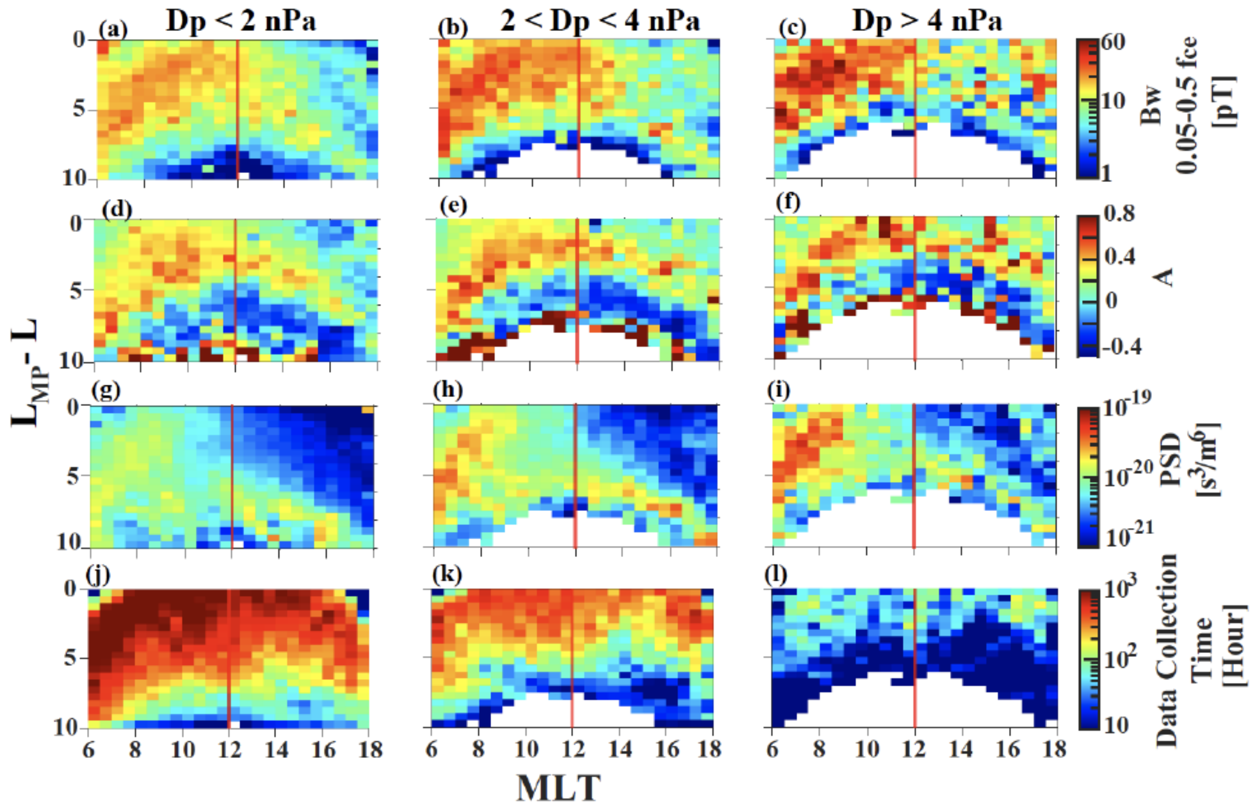


**Figure 5.** The same format as Figure 4, but for LB waves and electrons at 14 keV.

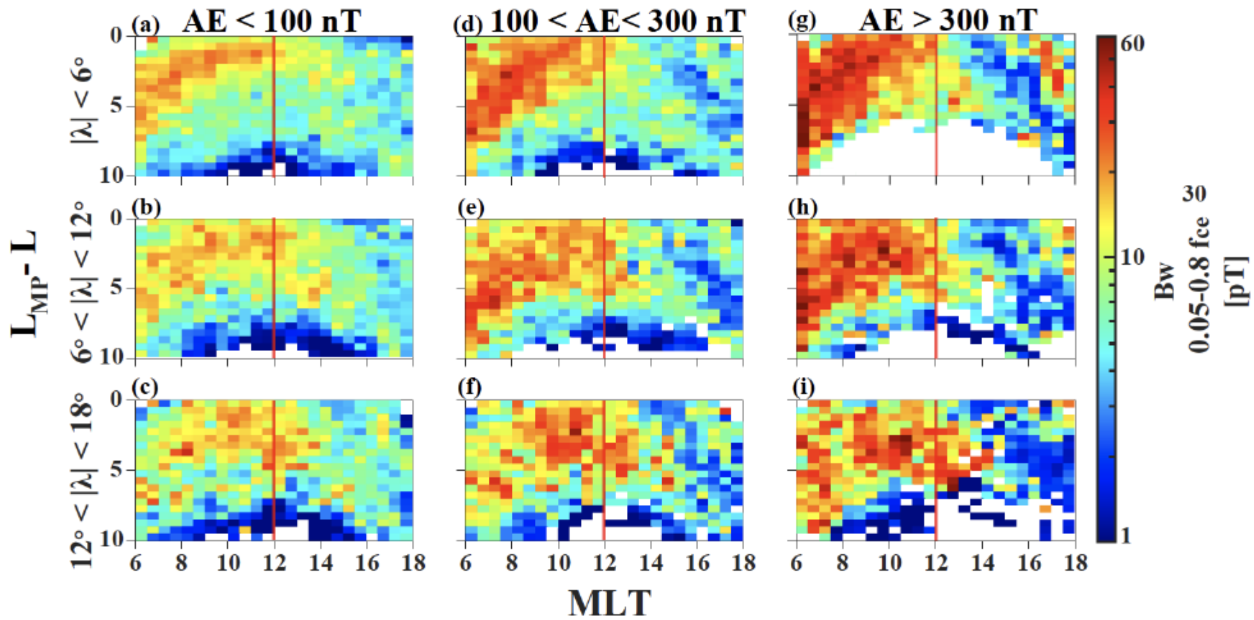


**Figure 6**. Dayside whistler-mode wave amplitudes (over the frequency range of 0.05–0.8 $f_{ce}$) as functions of MLT and $L_{mp}$-L at three different magnetic latitudes (sorted by rows) under different AE conditions (sorted by columns).

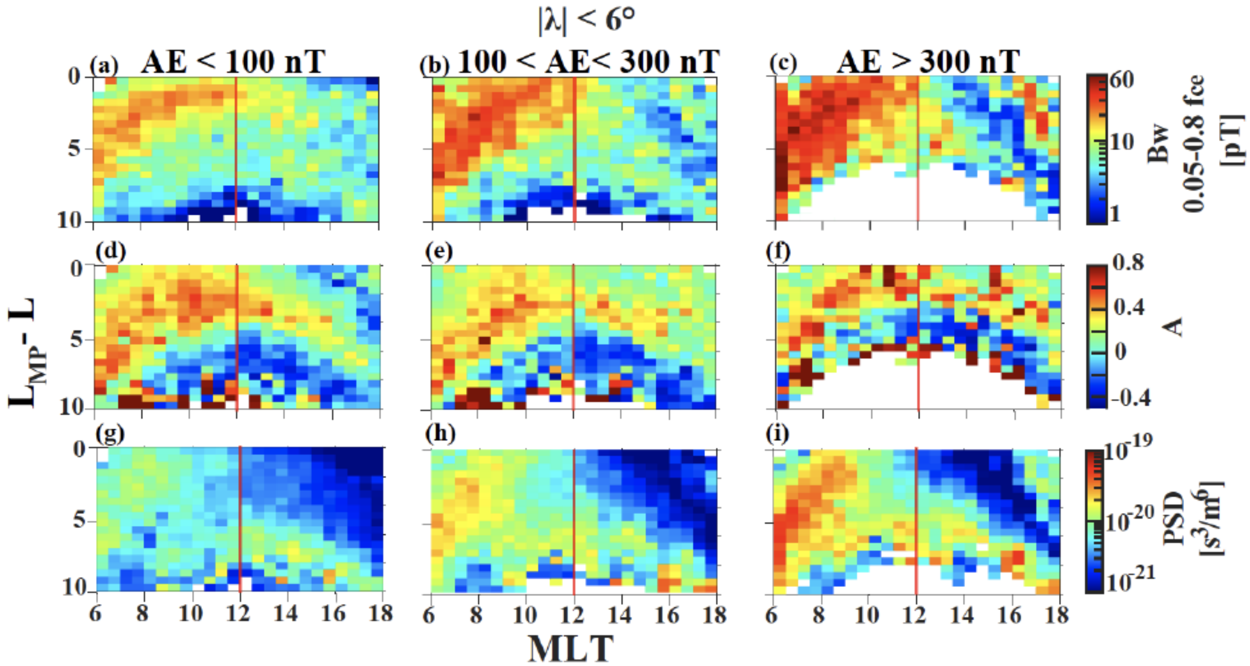


**Figure 7.** The distribution of dayside whistler-mode waves and electrons as functions of MLT and $L_{MP}$-L near the equatorial plane ($|\lambda| < 6°$). (a–c) Wave amplitude; (d–f) 14 keV electron anisotropy; and (g–i) omni-directional electron PSD under various AE conditions.

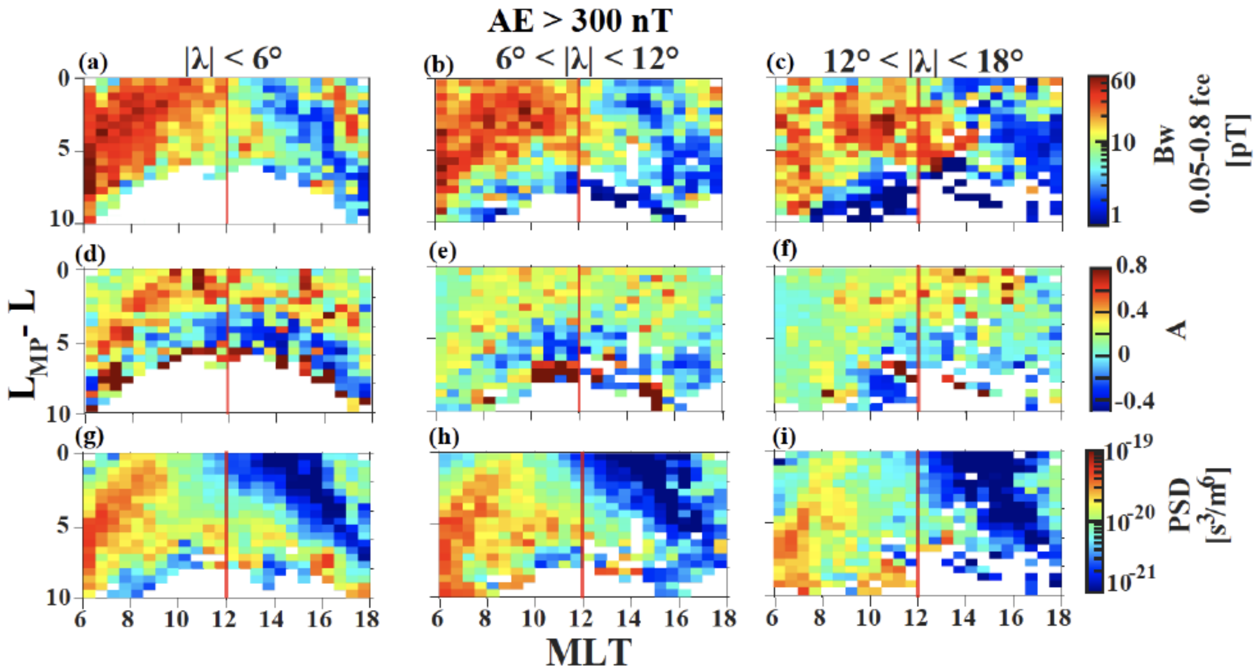


**Figure 8**. The distribution of dayside whistler-mode waves and electrons as functions of MLT and $L_{MP}$-L under active conditions (AE > 300 nT). (a–c) Wave amplitude; (d–f) 14 keV electron anisotropy; and (g–i) the corresponding omni-directional PSD, at different magnetic latitudes sorted by column.

**Figure 1.**

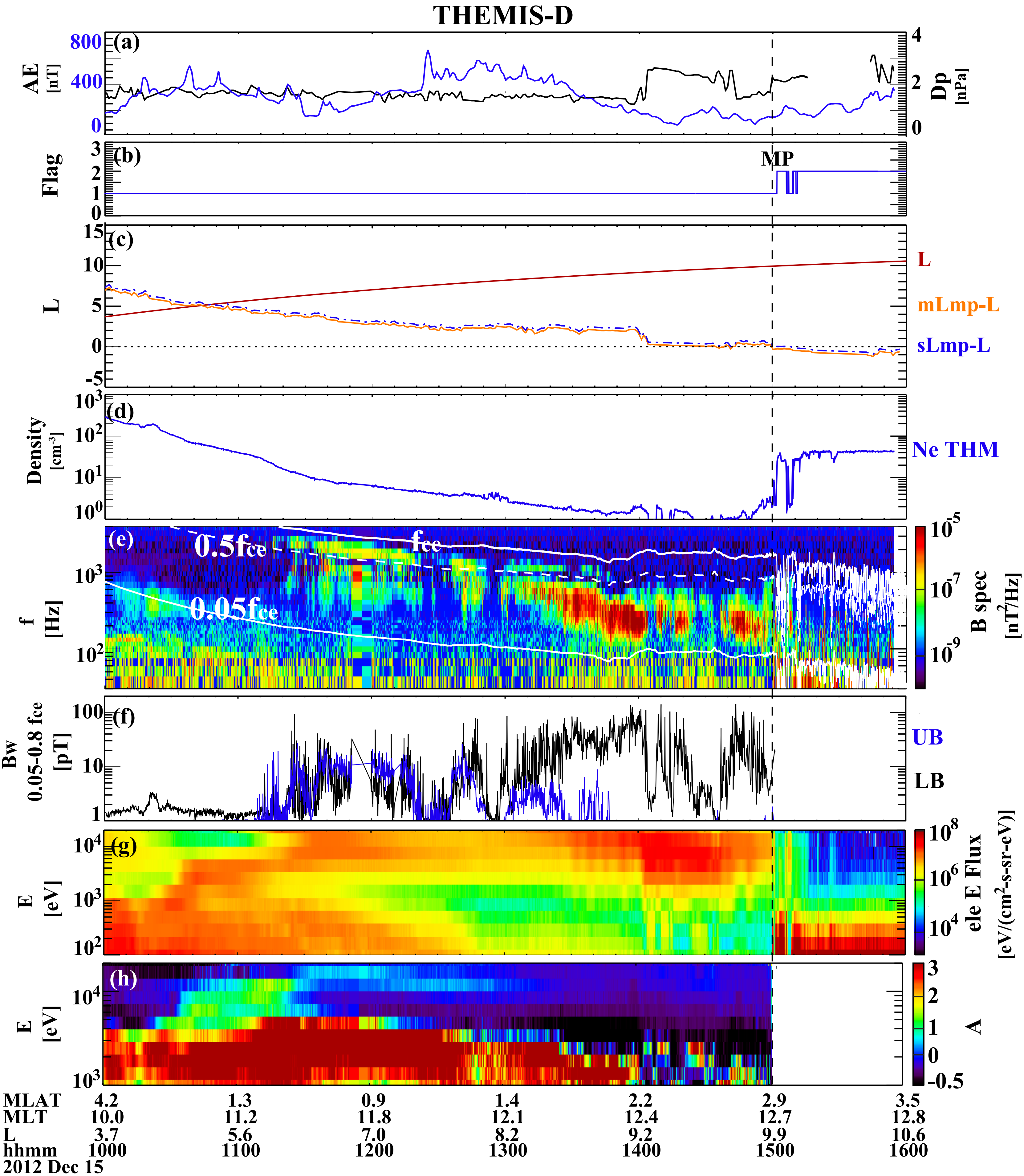
THEMIS-D
(a)
AE [nT]
800
400
0
Dp [nPa]
4
2
0
(b)
Flag
MP
(c)
L
mLmp-L
sLmp-L
(d)
Density [cm⁻³]
Ne THM
(e)
f [Hz]
0.5fce
fce
0.05fce
B spec [nT²/Hz]
(f)
Bw 0.05-0.8 fce [pT]
UB
LB
(g)
E [eV]
ele E Flux [eV/(cm²-s-sr-eV)]
(h)
E [eV]
A
MLAT 4.2 1.3 0.9 1.4 2.2 2.9 3.5
MLT 10.0 11.2 11.8 12.1 12.4 12.7 12.8
L 3.7 5.6 7.0 8.2 9.2 9.9 10.6
hhmm 1000 1100 1200 1300 1400 1500 1600
2012 Dec 15

**Figure 2.**

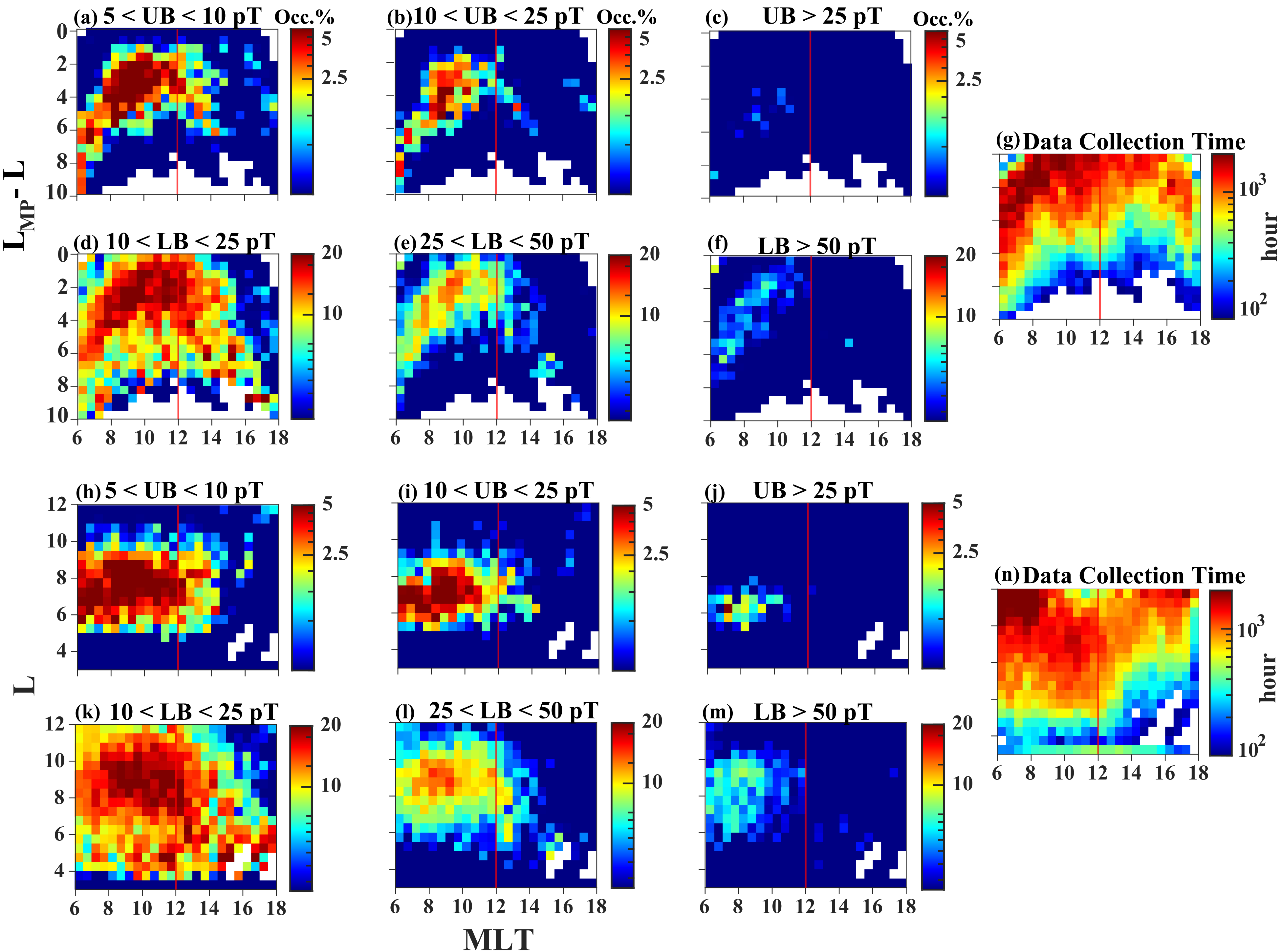

(a) 5 < UB < 10 pT
Occ.%
(b)10 < UB < 25 pT
Occ.%
(c) UB > 25 pT
Occ.%
(d) 10 < LB < 25 pT
(e) 25 < LB < 50 pT
(f) LB > 50 pT
(g) Data Collection Time
hour
$L_{MP}$ - L
(h) 5 < UB < 10 pT
(i) 10 < UB < 25 pT
(j) UB > 25 pT
(k) 10 < LB < 25 pT
(l) 25 < LB < 50 pT
(m) LB > 50 pT
(n) Data Collection Time
hour
L
MLT

**Figure 3.**

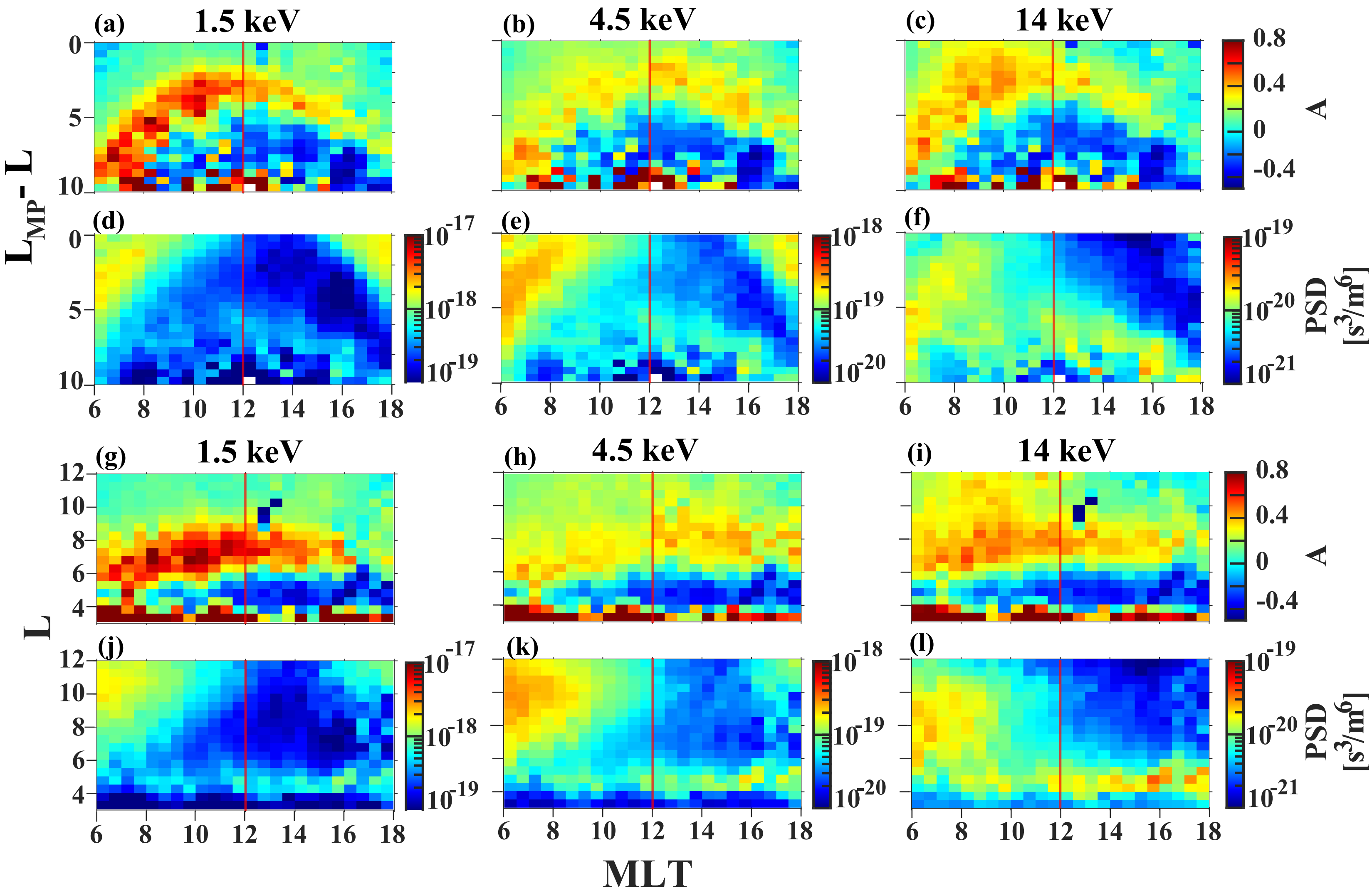

(a) 1.5 keV
(b) 4.5 keV
(c) 14 keV
(d)
(e)
(f)
(g) 1.5 keV
(h) 4.5 keV
(i) 14 keV
(j)
(k)
(l)
$L_{MP}$ - L
L
MLT
A
PSD $[s^3/m^6]$

**Figure 4.**

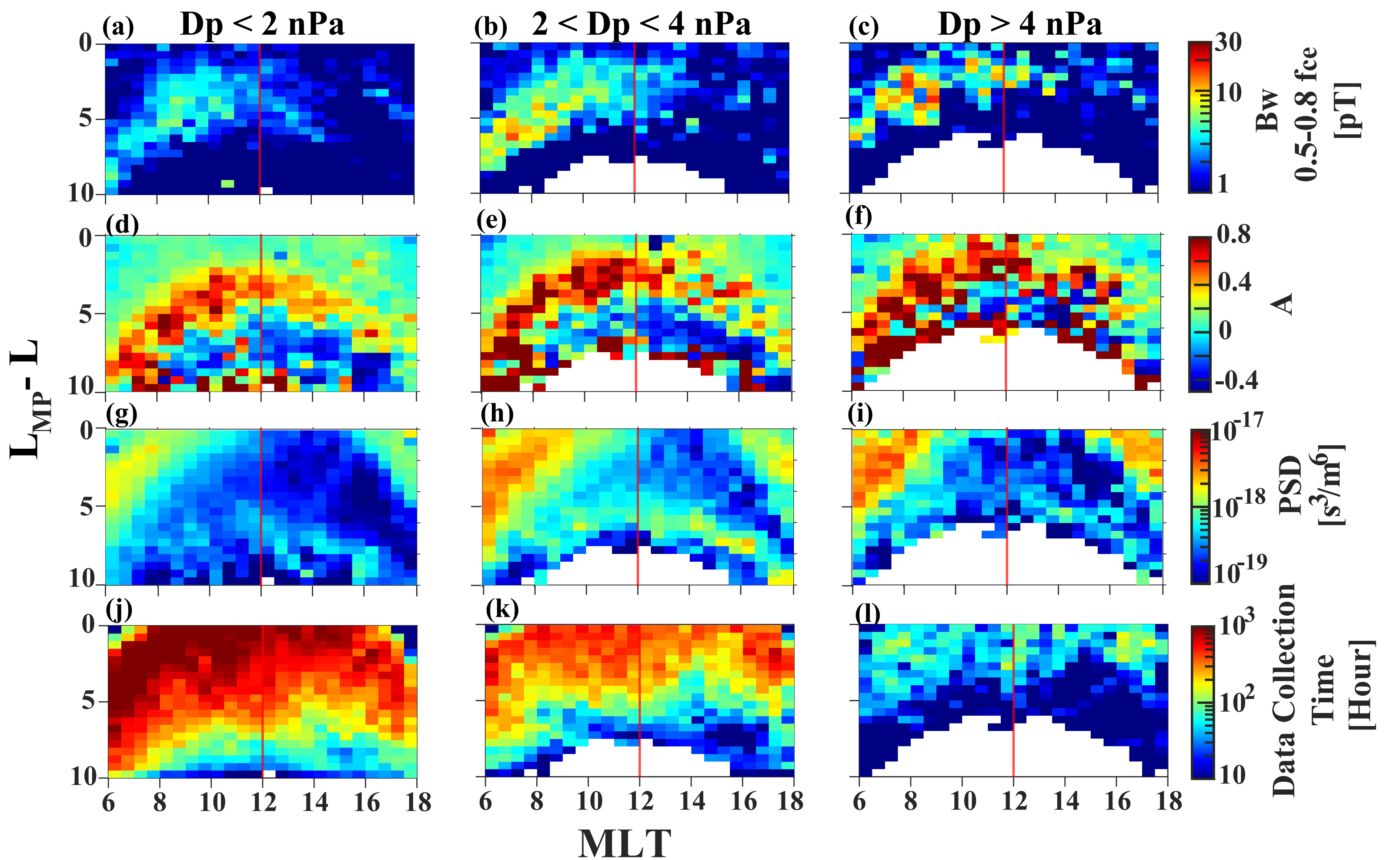

(a) Dp < 2 nPa
(b) 2 < Dp < 4 nPa
(c) Dp > 4 nPa
(d)
(e)
(f)
(g)
(h)
(i)
(j)
(k)
(l)
Bw 0.5-0.8 fce [pT]
A
PSD [s^3/m^6]
Data Collection Time [Hour]
L_MP - L
MLT

**Figure 5.**

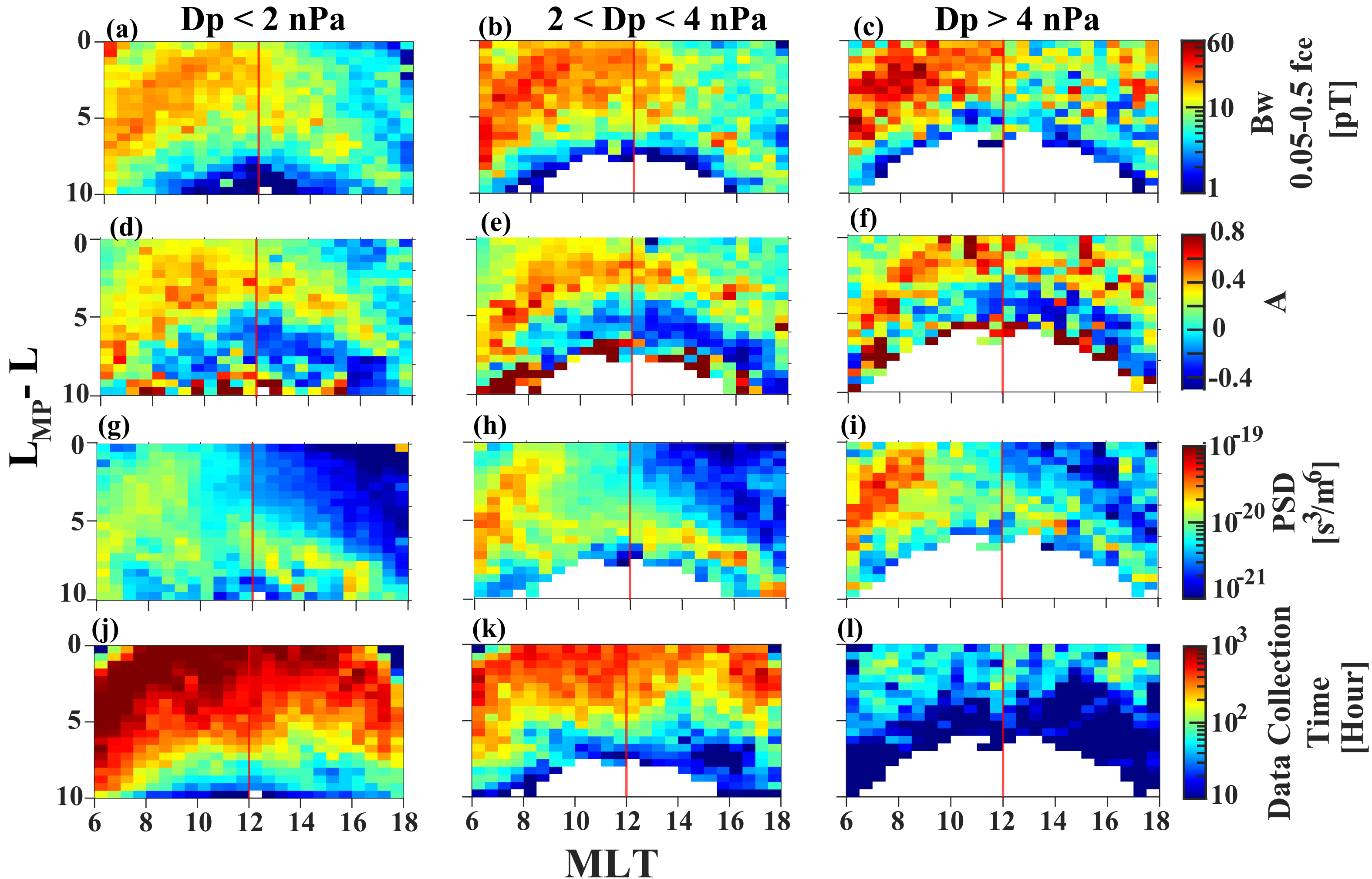

Dp < 2 nPa
2 < Dp < 4 nPa
Dp > 4 nPa
(a)
(b)
(c)
(d)
(e)
(f)
(g)
(h)
(i)
(j)
(k)
(l)
Bw 0.05-0.5 fce [pT]
A
PSD [s^3/m^6]
Data Collection Time [Hour]
L_MP - L
MLT

**Figure 6.**

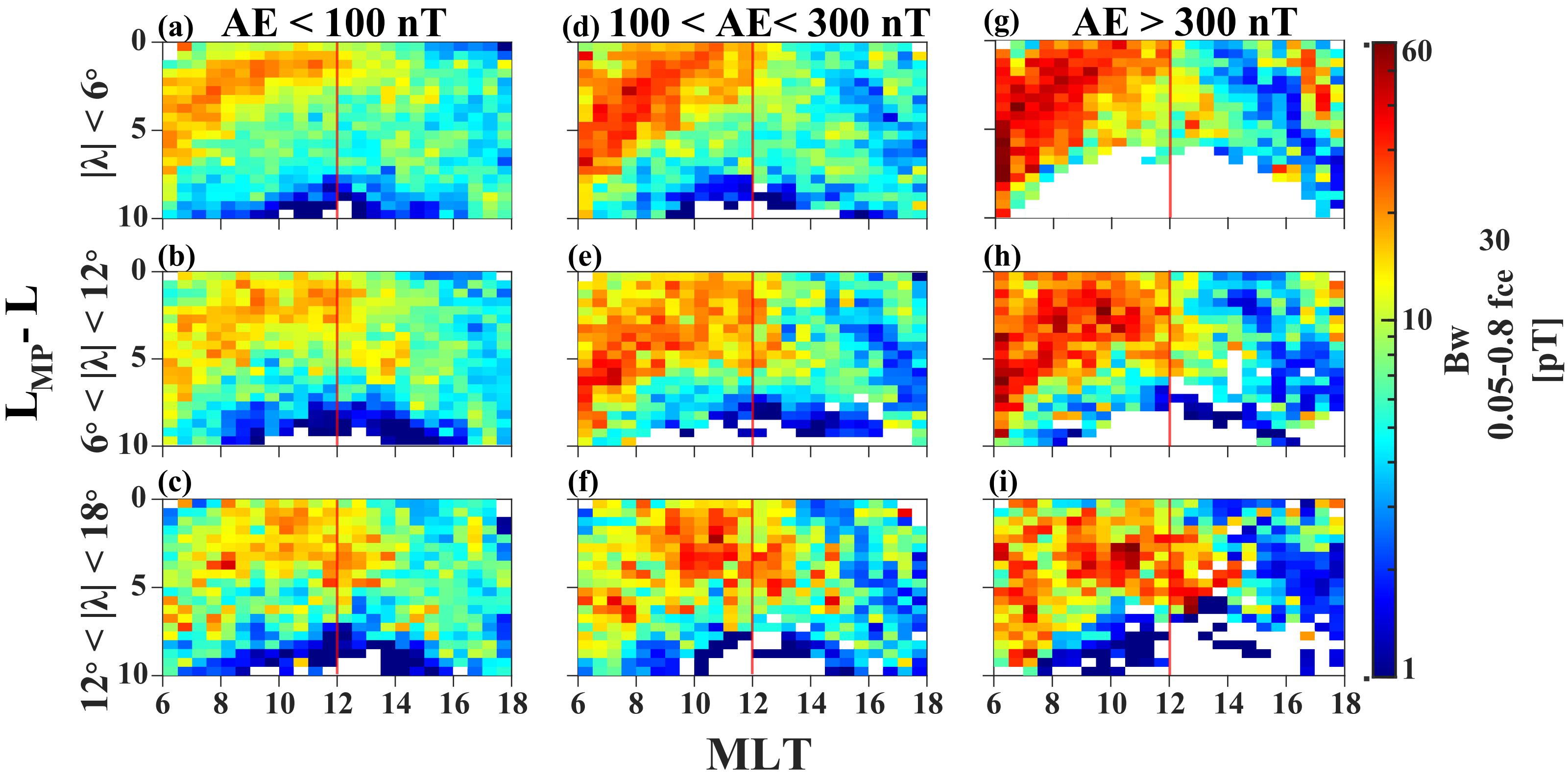

(a) AE < 100 nT
(d) 100 < AE< 300 nT
(g) AE > 300 nT
(b)
(e)
(h)
(c)
(f)
(i)
$L_{MP}$ - L
|λ| < 6°
6° < |λ| < 12°
12° < |λ| < 18°
0
5
10
6
8
10
12
14
16
18
MLT
60
30
10
1
Bw
0.05-0.8 fce
[pT]

**Figure 7.**

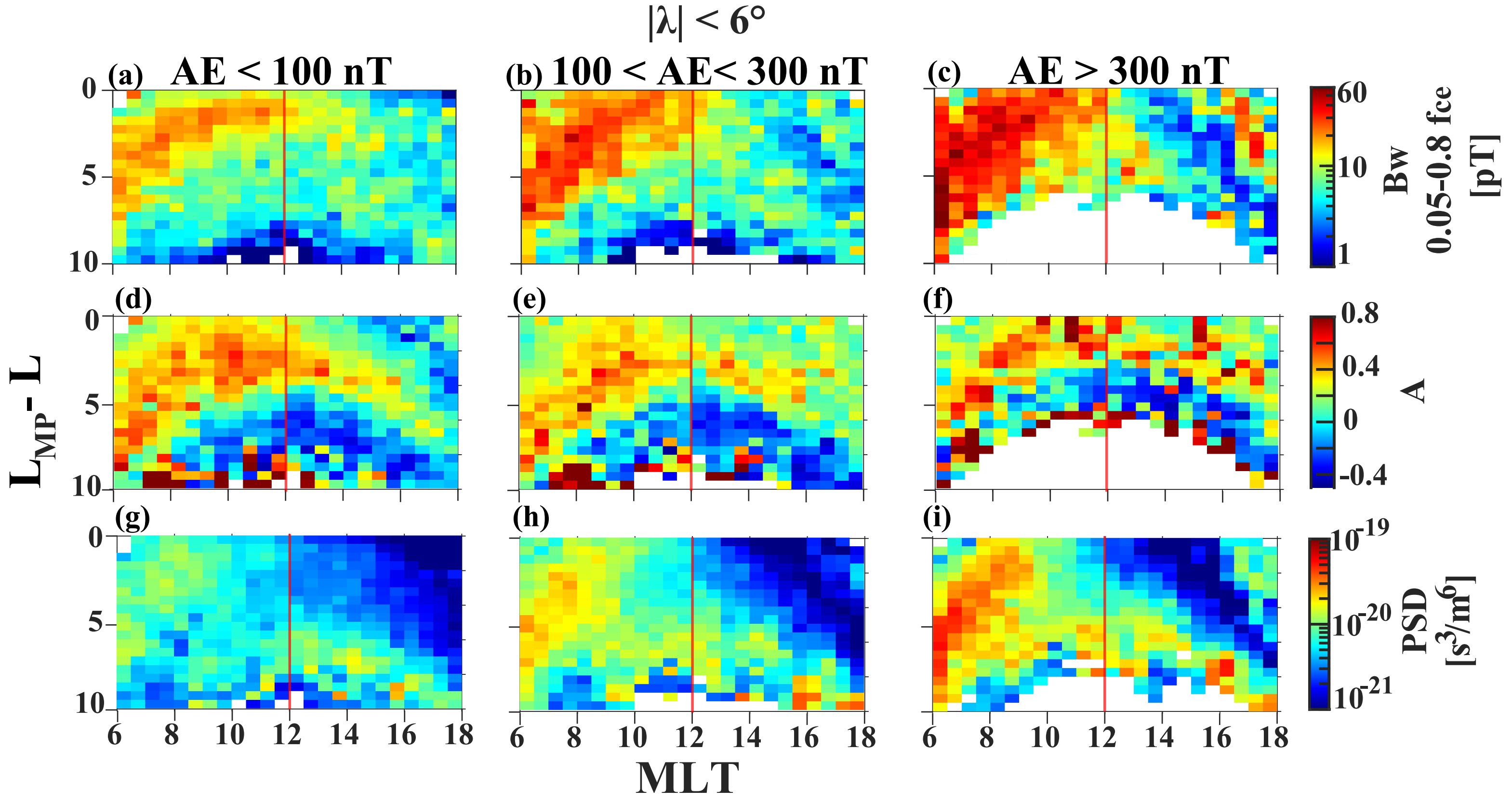

|λ| < 6°
(a) AE < 100 nT
(b) 100 < AE< 300 nT
(c) AE > 300 nT
(d)
(e)
(f)
(g)
(h)
(i)
$L_{MP}$ - L
MLT
Bw 0.05-0.8 fce [pT]
A
PSD [s³/m⁶]

**Figure 8.**

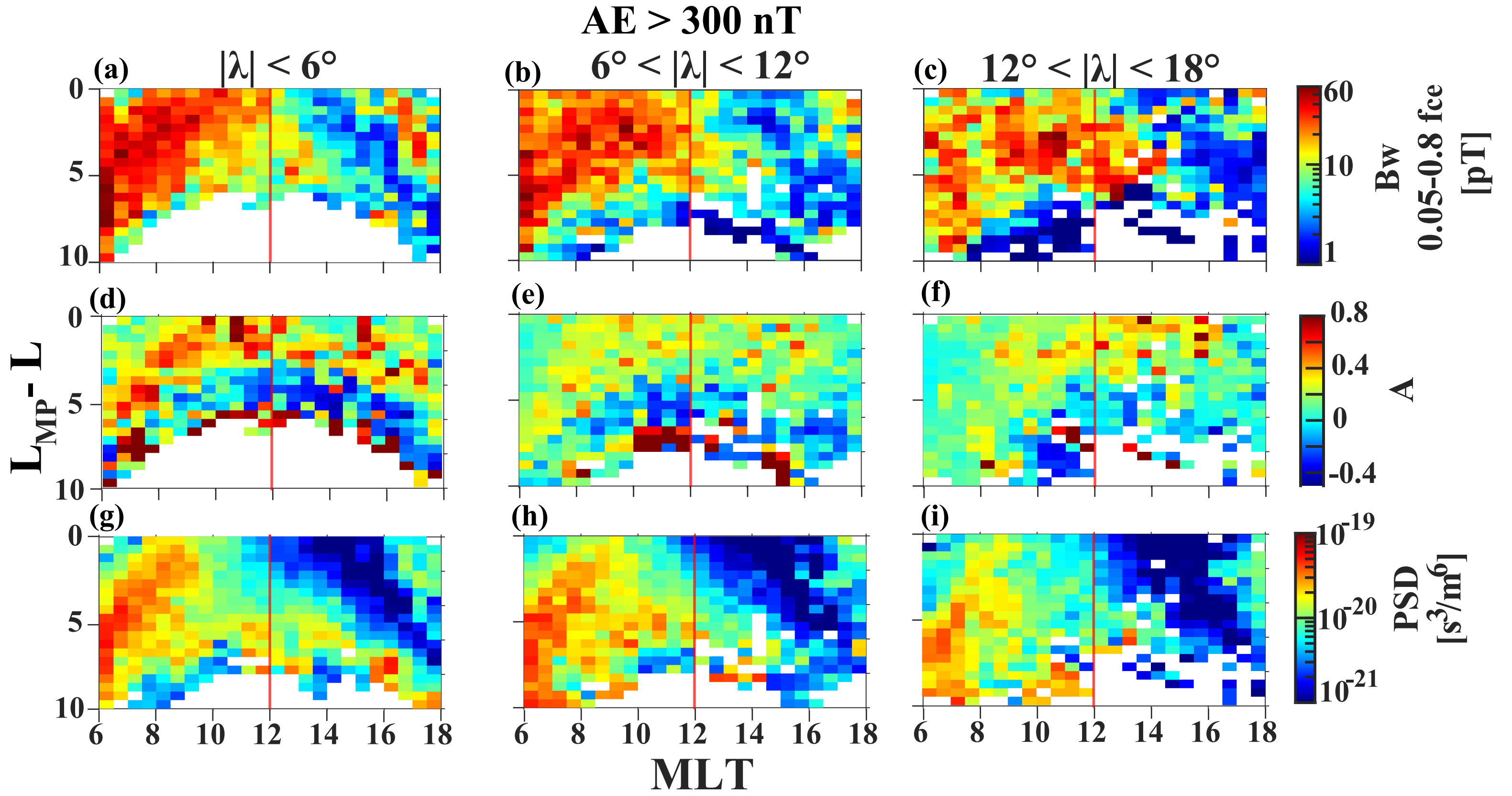
AE > 300 nT
(a)
|λ| < 6°
(b)
6° < |λ| < 12°
(c)
12° < |λ| < 18°
(d)
(e)
(f)
(g)
(h)
(i)
L_MP - L
MLT
Bw
0.05-0.8 fce
[pT]
A
PSD
[s^3/m^6]
60
10
1
0.8
0.4
0
-0.4
10^-19
10^-20
10^-21
0
5
10
6
8
10
12
14
16
18